The Astrophysical Journal, 657:810–837, 2007 March 10

INFRARED EMISSION FROM INTERSTELLAR DUST. IV. THE SILICATE-GRAPHITE-PAH MODEL IN THE POST-*SPITZER* ERA

B. T. Draine
Princeton University Observatory, Peyton Hall, Princeton, NJ; draine@astro.princeton.edu

and

Aigen Li
Department of Physics and Astronomy, University of Missouri, Columbia, MO; lia@missouri.edu
Received 2006 July 27; accepted 2006 October 19

ABSTRACT

IR emission spectra are calculated for dust heated by starlight, for mixtures of amorphous silicate and graphitic grains, including varying amounts of PAH particles. The models are constrained to reproduce the average Milky Way extinction curve. The calculations include the effects of single-photon heating. Updated IR absorption properties for the PAHs are presented that are consistent with observed emission spectra, including those newly obtained by *Spitzer*. We find a size distribution for the PAHs giving emission band ratios consistent with the observed spectra of the Milky Way and other galaxies. Emission spectra are presented for a wide range of starlight intensities. We calculate how the efficiency of emission into different IR bands depends on PAH size; the strong 7.7 μm emission feature is produced mainly by PAH particles containing $<10^3$ C atoms. We also calculate how the emission spectrum depends on U, the starlight intensity relative to the local interstellar radiation field. The submillimeter and far-infrared emission is compared to the observed emission from the local interstellar medium. Using a simple distribution function, we calculate the emission spectrum for dust heated by a distribution of starlight intensities, such as occurs within galaxies. The models are parameterized by the PAH mass fraction $q_{\rm PAH}$, the lower cutoff $U_{\rm min}$ of the starlight intensity distribution, and the fraction γ of the dust heated by starlight with $U > U_{\rm min}$. We present graphical procedures using *Spitzer* IRAC and MIPS photometry to estimate the parameters $q_{\rm PAH}$, $U_{\rm min}$, and γ, the fraction $f_{\rm PDR}$ of the dust luminosity coming from photodissociation regions with $U > 100$, and the total dust mass $M_{\rm dust}$.

Subject headings: dust, extinction — infrared: galaxies — infrared: ISM — radiation mechanisms: thermal

1. INTRODUCTION

Interstellar dust in galaxies absorbs energy from starlight; this absorbed energy is then reradiated at infrared (IR) and far-IR (FIR) wavelengths. The unprecedented sensitivity of *Spitzer Space Telescope* (Werner et al. 2004b) allows this IR emission to be measured for a wide range of galaxy sizes and morphologies. The spectral properties of the IR emission from dust allow one to infer the composition of the dust, the size distribution of the dust particles, the intensity of the starlight that is heating the dust, and the total mass of dust.

Deducing the dust properties and starlight intensity is by no means direct or straightforward. To start, one needs to assume a provisional dust model with the physical nature of the dust (composition, geometry, and size distribution) fully specified. One then tries to constrain the grain properties by comparing model predictions with observations (e.g., interstellar extinction, scattering, polarization, IR and microwave emission, and interstellar depletions).

Various models have been proposed for interstellar dust. The models fall into three broad categories: (1) the silicate-graphite model (Mathis et al. 1977; Draine & Lee 1984; Kim et al. 1994) and its natural extension—the silicate-graphite-PAH model (Siebenmorgen & Krügel 1992; Li & Draine 2001b, hereafter LD01; Weingartner & Draine 2001a, hereafter WD01); (2) the silicate core carbonaceous mantle model (Désert et al. 1990; Jones et al. 1990; Li & Greenberg 1997); and (3) the composite model, which assumes the dust to be low-density aggregates of small silicate and carbonaceous particles (Mathis & Whiffen 1989; Mathis 1996; Zubko et al. 2004). The core-mantle model is challenged by the nondetection of polarization in the 3.4 μm C—H aliphatic hydrocarbon feature on sight lines where the 9.7 μm Si—O silicate band is observed to be polarized (Chiar et al. 2006; Mason et al. 2007; see also Adamson et al. 1999; Li & Greenberg 2002). The original composite model proposed by Mathis & Whiffen (1989), with ~80% of the grain volume consisting of vacuum, may have too flat an FIR emissivity to explain the observational data (Draine 1994). The updated version of the composite model of Mathis (1996) assumes a vacuum fraction ~45% in order to make economical use of the available carbon to account for the observed extinction while satisfying the "subsolar" interstellar abundance budget suggested by Snow & Witt (1996). However, Dwek (1997) argues that this dust model emits too much in the FIR in comparison with observations. The latest version of the composite model put forward by Zubko et al. (2004) aims at reproducing the observed interstellar extinction and IR emission within a subsolar abundance budget. The ability of composite grain models to reproduce the observed extinction within subsolar abundance constraints was recently challenged by Li (2005) based on the Kramers-Kronig relations.[1]

[1] Total (gas+dust) interstellar abundances remain uncertain. The most recent determination of the solar oxygen abundance, $({\rm O/H})_\odot = 10^{-3.34\pm0.05}$ (Asplund et al. 2004), is close to the value for B stars in the Orion association, ${\rm O/H} = 10^{-3.31\pm0.03}$ (Cunha et al. 2006). The warm ISM gas has ${\rm O/H} = 10^{-3.41\pm0.01}$ (Cartledge et al. 2006), consistent with ~20% of the oxygen being in silicate grains. For "refractory" elements such as Mg, Si, and Fe, however, partial separation of dust and gas by processes such as radiation pressure, ambipolar diffusion, and gravitational sedimentation in the process of star formation could result in stellar abundances differing from interstellar abundances (Snow 2000; Draine 2004). Photospheric abundances may therefore not be a reliable indicator of interstellar abundances for the elements that form refractory grains.

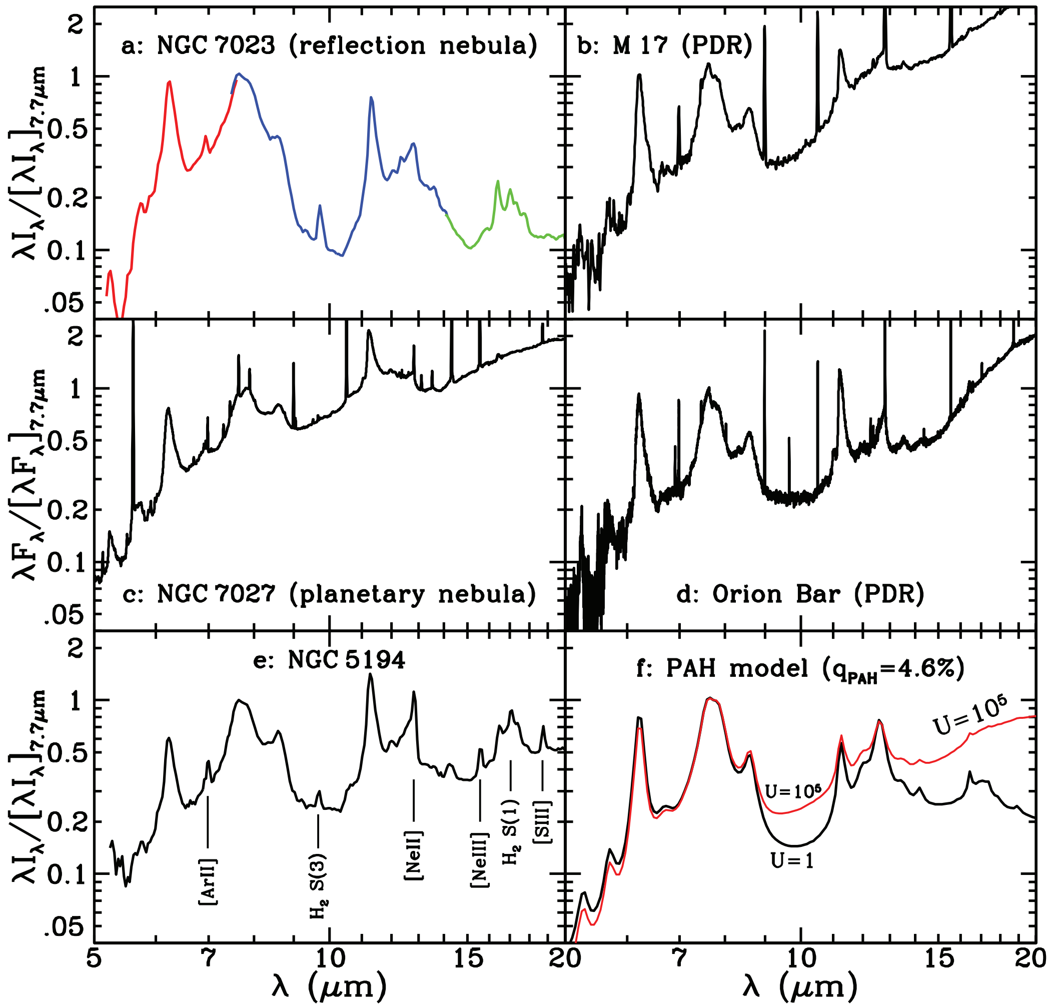

FIG. 1.—Observed 5–20 μm spectra for (*a*) reflection nebula NGC 7023 (Werner et al. 2004a); (*b*) Orion Bar PDR (Verstraete et al. 2001); (*c*) M17 PDR (Peeters et al. 2005); (*d*) planetary nebula NGC 7027 (van Diedenhoven et al. 2004); (*e*) Seyfert galaxy NGC 5194 (Smith et al. 2007). Also shown (*f*) is the emission calculated for the present dust model with $q_{PAH} = 4.6\%$, illuminated by the local diffuse starlight with $U = 1$ and 10^5 (see Fig. 13).

In this paper we calculate the IR emission expected from a specific physical model of interstellar dust: the silicate-graphite-PAH model. In this model, the dust is assumed to consist of a mixture of carbonaceous grains and amorphous silicate grains, with size distributions that are consistent with the observed wavelength-dependent extinction in the local Milky Way (WD01), including different amounts of polycyclic aromatic hydrocarbon (PAH) material.

Spectroscopic observations with the *Infrared Space Observatory* (*ISO*) revealed the rich spectrum of PAHs (see, e.g., Beintema et al. 1996; Tielens et al. 1999; Joblin et al. 2000), conspicuous in the spectra of planetary nebulae, photodissociation regions (PDRs), and entire galaxies (see Fig. 1). The model presented here posits "astro-PAH" absorption properties that are consistent with spectroscopic observations of PAH emission from dust in nearby galaxies (Smith et al. 2007). The model calculations show how the IR emission depends on the PAH abundance and also on the intensity of starlight heating the dust. Comparison of models to infrared photometry obtained with *Spitzer* allows one to estimate PAH abundances, starlight intensities, and total dust masses.

With new laboratory data (particularly the near-IR absorption spectra of PAH ions measured by Mattioda et al. 2005b) and *Spitzer* spectroscopic data (with new PAH features discovered; Smith et al. 2004a, 2007; Werner et al. 2004a; and with the familiar 7.7, 8.6, and 11.3 μm features resolved into several subfeatures; Smith et al. 2007), we update in § 2 the cross sections $C_{abs}(\lambda)$ that we previously assumed for the PAH particles[2] (LD01). We distinguish the PAHs by two charge states: either neutral (PAH^0) or ionized ($PAH^{\pm}$). We assume that multiply charged (both positively and negatively) PAHs all have the same cross sections as those of singly charged cations. The resulting astro-PAH absorption cross sections do not represent any specific material but should approximate the actual absorption properties of the PAH mixture in interstellar space.

In § 3 we show examples of temperature distribution functions for both neutral and ionized PAHs heated by starlight. These temperature distribution functions are then used to calculate emission spectra for individual particles in § 4, which are in turn used to prepare a plot (see Fig. 6 below) showing how the efficiency of emitting into different emission features depends on the PAH size.

When we observe emission from a region in the Milky Way or another galaxy, there will always be a mixture of dust types and

[2] Note that "PAH particles," "PAH grains," and "PAH molecules" are synonymous.

sizes present. We consider the emission from a specific set of dust mixtures, as described in § 5. All the dust mixtures considered here are consistent with the observed "average" extinction curve for diffuse regions in the local Milky Way, but they differ from one another in the assumed abundance of small PAH particles. In § 6 we show that the FIR and submillimeter emission calculated for the model is consistent with the *Cosmic Background Explorer* (*COBE*) FIRAS observations of emission from dust in the local Milky Way. In § 7 we show that the calculated IRAC band ratios appear to be consistent with the spectrum of diffuse emission from the Milky Way, as determined by Flagey et al. (2006) from *Spitzer* observations.

The long-wavelength emission from the dust model depends on the intensity of the starlight heating the dust. It will often be the case that the region observed (e.g., an entire star-forming galaxy) will include dust heated by a wide range of starlight intensities. In § 8 we describe a simple parametric model for the distribution of the dust mass between regions with starlight intensities ranging from low to very high. We show in § 9 how observations in the three MIPS bands (24, 71, and 160 μm) plus the 3.6 and 7.9 μm IRAC bands[3] can be used to estimate the parameters describing the distribution of starlight intensities, as well as the fraction $q_{\rm PAH}$ of the total dust mass that is in PAHs, thereby allowing estimation of the total dust mass $M_{\rm dust}$ in the emitting region. A reader interested primarily in applying the results of this paper to interpretation of IRAC and MIPS observations may wish to proceed directly to § 9.

The results of the paper are discussed in § 10 and summarized in § 11.

2. PAH CROSS SECTIONS: POST-*SPITZER* ERA

The strong and ubiquitous interstellar emission features observed at 3.3, 6.2, 7.7, 8.6, and 11.3 μm almost certainly arise from vibrational modes of PAH material, with C—H stretching modes producing the 3.3 μm feature, C—H bending modes producing the in-plane 8.6 μm and out-of-plane 11.3 μm features, and C—C stretching and bending modes producing emission features at 6.2 and 7.7 μm and longer wavelengths (Leger & Puget 1984; Allamandola et al. 1985).[4]

To reproduce this emission, a dust model must include a substantial population of ultrasmall grains or large molecules with the vibrational properties of PAH material and with sizes such that single-photon heating can excite the observed vibrational emission. Because the exact composition of the interstellar PAH material is unknown, and also because laboratory knowledge of the optical properties of PAHs is very limited, it is necessary to make assumptions regarding the absorption cross sections of the PAH particles.

The approach taken here to modeling the PAHs is to try to find optical properties for astro-PAH material that appear to be physically reasonable (i.e., band strengths within the range measured for PAHs in the laboratory), in order to estimate the sizes and abundance of interstellar PAHs that would be consistent with the observed emission spectra. To this end, we adopt feature profiles that are based on astronomical observations. At wavelengths $\lambda > 5.5$ μm, the spectra for the central regions of galaxies in the SINGS galaxy sample (Smith et al. 2007) provide observed profiles for the spectral features that the present model attempts to mimic. We follow LD01 in describing the PAH vibrational resonances by Drude profiles (components $j = 6$–30 in Table 1),[5]

$$\Delta C_{\rm abs}(\lambda) = N_{\rm C} \sum_{j=1}^{30} \frac{2}{\pi} \frac{\gamma_j \lambda_j \sigma_{{\rm int},j}}{\left(\lambda/\lambda_j - \lambda_j/\lambda\right)^2 + \gamma_j^2}, \qquad (1)$$

but with new profile parameters, adjusted to closely resemble the observed profiles. The profile parameters are given in Table 1, where λ_j, $\gamma_j \lambda_j$, and $\sigma_{\rm int} \equiv \int \sigma_{\rm abs}\, d\lambda^{-1}$ are, respectively, the peak wavelength, the FWHM, and the integrated strength per C atom of the jth Drude resonance. The features in Table 1 and their identifications have been discussed previously (see, e.g., Tielens 2005), with Smith et al. (2007) providing a comprehensive study of the 5–35 μm emission from galaxies. We assume the PAH particles to have absorption cross sections per carbon atom $C_{\rm abs}(\lambda)/N_{\rm C}$ equal to those adopted by LD01 (see eqs. [5]–[11] of that paper), except for the following changes:

1. For PAH ions, we add additional absorption in the near-IR as recommended by Mattioda et al. (2005a). This consists of a "continuum" term

$$\frac{\Delta C_{\rm abs}(\lambda)}{N_{\rm C}} = 3.5 \times 10^{-19-1.45/x} \exp\left(-0.1x^2\right) \text{ cm}^2 \qquad (2)$$

for ions, with $x \equiv (\lambda/\mu{\rm m})^{-1}$. Because PAH ions were already assumed to absorb strongly at $\lambda \lesssim 0.8$ μm, this additional absorption is numerically insignificant for $\lambda \lesssim 0.8$ μm; the factor $\exp(-0.1x^2)$ has been added simply to force this term to go smoothly to zero as $\lambda \rightarrow 0$.

2. For PAH ions, we add near-IR resonances at wavelengths 1.05 and 1.26 μm plus a negative "resonance" term at 1.905 μm to suppress absorption in the 1.8–2.0 μm region, as recommended by Mattioda et al. (2005a); the three features are represented by Drude profiles, with parameters as given in Table 1. The negative term at $\lambda = 1.905$ μm ($j = 5$) was suggested by the recent laboratory data of Mattioda et al. (2005b). Removal of this term has a negligible effect on the heating or cooling rates of PAHs except in regions illuminated by very cool stars ($T_{\rm eff} \lesssim 1500$ K) or in regions where the PAHs are excited to unusually high temperatures ($T \gtrsim 1500$ K).

3. Small changes have been made to central wavelengths and feature widths (e.g., $\lambda_j = 6.20 \rightarrow 6.22$ μm and $\gamma_j = 0.032 \rightarrow 0.0284$ for the feature near 6.2 μm, $\lambda_j = 11.9 \rightarrow 11.99$ μm and $\gamma_j = .025 \rightarrow 0.050$ for the feature near 12 μm, and $\lambda_j = 12.7 \rightarrow 12.61$ μm and $\gamma_j = .024 \rightarrow 0.0435$ for the feature near 12.7 μm)

[3] The IRAC and MIPS bands are often referred to using nominal wavelengths 3.6, 4.5, 5.8, 8.0, 24, 70, and 160 μm. However, to two significant digits, the effective wavelengths of IRAC bands 3 and 4 are 5.7 and 7.9 μm (IRAC Data Handbook, ver. 3.0), and that of MIPS band 2 is 71 μm (MIPS Data Handbook ver. 3.2), and we use these wavelengths to refer to the bands.

[4] Other carriers have also been proposed, including hydrogenated amorphous carbon (HAC; Jones et al. 1990), quenched carbonaceous composite (QCC; Sakata et al. 1987), coal (Papoular et al. 1993), hydrogenated fullerenes (Webster 1993), and nanodiamonds (Jones & d'Hendecourt 2000). The HAC, QCC, and coal hypotheses assume that the emission arises following photon absorption in small thermally isolated aromatic units within or attached to these bulk materials (Duley & Williams 1981). However, it does not appear possible to confine the absorbed photon energy within these aromatic "islands" for the time $\gtrsim 10^{-3}$ s required for the thermal emission process (see Li & Draine 2002a). Free-flying fullerenes and nanodiamonds have the required small heat capacity, but (1) there are strong upper limits on the abundance of C_{60} and C_{60}^+ (Moutou et al. 1999), and (2) although not ruled out, there is little spectroscopic evidence for hydrogenated nanodiamonds in the ISM.

[5] Boulanger et al. (1998) have shown that Lorentz profiles provide good fits to the PAH emission features from the NGC 7023 reflection nebula and the ρ Oph molecular cloud. The Drude profile closely resembles a Lorentz profile (both have more extended wings than a Gaussian profile). We favor the Drude profile as it is expected for classical damped harmonic oscillators.

TABLE 1
PAH Resonance Parameters

j	λ_j (μm)	γ_j	$\sigma_{\text{int},j} \equiv \int \sigma_{\text{abs},j}\, d\lambda^{-1}$ Neutral (10^{-20} cm/C)	Ionized (10^{-20} cm/C)	Tentative Identification
1	0.0722	0.195	7.97×10^7	7.97×10^7	$\sigma \rightarrow \sigma^*$ transition in aromatic C
2	0.2175	0.217	1.23×10^7	1.23×10^7	$\pi \rightarrow \pi^*$ transition in aromatic C
3	1.050	0.055	0	2.0×10^4	Weak electronic transition(s) in PAH cations
4	1.260	0.11	0	0.078	Weak electronic transition(s) in PAH cations
5	1.905	0.09	0	−146.5	?
6	3.300	0.012	394(H/C)	89.4(H/C)	Aromatic C—H stretch
7	5.270	0.034	2.5	20	C—H bend + C—H stretch combination mode
8	5.700	0.035	4	32	C—H bend + C—H stretch combination mode
9	6.220	0.030	29.4	235	Aromatic C—C stretch (in-plane)
10	6.690	0.070	7.35	59	?
11	7.417	0.126	20.8	181	Aromatic C—C stretch
12	7.598	0.044	18.1	163	Aromatic C—C stretch
13	7.850	0.053	21.9	197	C—C stretch + C—H bending
14	8.330	0.052	6.94(H/C)	48(H/C)	C—C stretch + C—H bending?
15	8.610	0.039	27.8(H/C)	194(H/C)	C—H in-plane bending
16	10.68	0.020	0.3(H/C)	0.3(H/C)	C—H out-of-plane bending, solo?
17	11.23	0.012	18.9(H/C)	17.7(H/C)	C—H out-of-plane bending, solo
18	11.33	0.032	52(H/C)	49(H/C)	C—H out-of-plane bending, solo
19	11.99	0.045	24.2(H/C)	20.5(H/C)	C—H out-of-plane bending, duo
20	12.62	0.042	35(H/C)	31(H/C)	C—H out-of-plane bending, trio
21	12.69	0.013	1.3(H/C)	1.3(H/C)	C—H out-of-plane bending, trio
22	13.48	0.040	8.0(H/C)	8.0(H/C)	C—H out-of-plane bending, quartet?
23	14.19	0.025	0.45	0.45	C—H out-of-plane bending, quartet?
24	15.90	0.020	0.04	0.04	?
25	16.45	0.014	0.5	0.5	C—C—C bending?
26	17.04	0.065	2.22	2.22	C—C—C bending?
27	17.375	0.012	0.11	0.11	C—C—C bending?
28	17.87	0.016	0.067	0.067	C—C—C bending?
29	18.92	0.10	0.10	0.17	C—C—C bending?
30	15	0.8	50	50	...

guided by spectra obtained recently by *Spitzer* (Smith et al. 2007).

4. The integrated strength $\sigma_{\text{int}} \equiv \int \sigma_{\text{abs}}\, d\lambda^{-1}$ of the 3.3 μm feature has been increased by a factor of 1.5 for neutrals and a factor of 2 for ions, to better agree with the range of values calculated for a number of PAHs (see Fig. 2).

5. Parameter σ_{int} for the 6.22 μm feature is 50% of the value in LD01.

6. The 7.7 μm complex is now composed of three components, at 7.417, 7.598, and 7.850 μm, with σ_{int} equal to 50% of the 7.7 μm feature in LD01.

7. Parameter σ_{int} of the 8.6 μm feature in LD01 is now shared by features at 8.330 and 8.610 μm, with σ_{int} equal to 50% of the 8.6 μm feature in LD01.

8. The 11.3 μm feature is now composed of features at 11.23 and 11.30 μm, with σ_{int} equal to 50% of the 11.3 μm feature in LD01.

9. The integrated strength σ_{int} of the 12.7 μm feature has been multiplied by 0.63 for both neutrals and ions relative to LD01.

10. Weak features have been added at 5.70, 6.69, 13.60, 14.19, 15.90, and 18.92 μm, as seen in spectra of star-forming galaxies in the Spitzer Infrared Nearby Galaxies Survey (SINGS; Smith et al. 2007). The 5.70 μm feature has previously been seen in planetary nebulae (Allamandola et al. 1989a) and PDRs (Verstraete et al. 1996; Peeters et al. 2004) and is presumed to be due to combination and overtone bands involving C—H out-of-plane bending modes.

11. A weak feature at 5.25 μm, seen in spectra of the M17 PDR and the Orion Bar (Verstraete et al. 1996; Peeters et al. 2004) and presumed to be due to C—H out-of-plane combination and overtone modes (Allamandola et al. 1989a), has been added.

12. The strength of the 16.4 μm feature has been multiplied by 0.14 relative to LD01.

13. A new emission complex near 17 μm has been added, composed of features at 17.038, 17.377, and 17.873 μm (Smith et al. 2004a, 2007; Werner et al. 2004a).

14. Emission features at 21.2 and 23.1 μm were seen in some laboratory samples (Moutou et al. 1996) and were therefore included by LD01 as examples of features that might be observed at $\lambda \gtrsim 20$ μm. However, the SINGS spectra (Smith et al. 2007) do not show any features at $\lambda > 19$ μm. The 21.2 and 23.1 μm features have therefore been eliminated in the new model.

15. LD01 included a broad absorption component with $\lambda_j = 26$ μm, $\gamma_j = 0.69$, and $\sigma_{\text{int}} = 18 \times 10^{-20}$ cm/C. This has been replaced by a broad absorption component with $\lambda_{27} = 15$ μm, $\gamma_{27} = 0.8$, and $\sigma_{\text{int}} = 50 \times 10^{-20}$ cm/C to provide continuum emission from 13 μm longward.

In general, PAHs and larger grains will not be spherical, but we characterize a grain of mass M by the effective radius a, defined to be the radius of an equal volume sphere: $a \equiv (3M/4\pi\rho)^{1/3}$, where amorphous silicate is assumed to have a mass density $\rho = 3.5$ g cm^{-3}, and carbonaceous grains are assumed to have a mass density due to graphitic carbon alone of $\rho = 2.2$ g cm^{-3}.

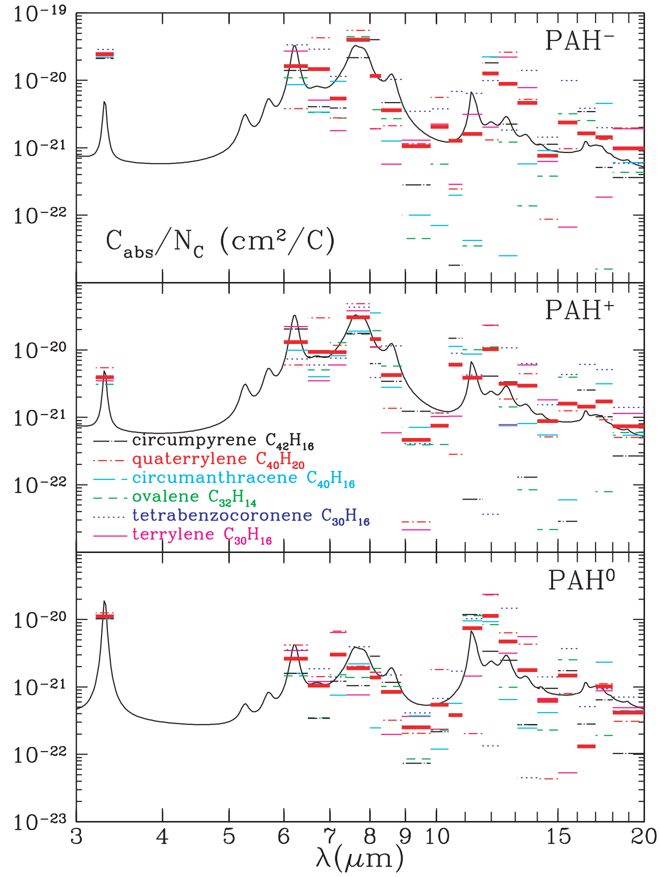

FIG. 2.—*Solid curve*: Adopted absorption cross section per C from eq. (5) with C/H $\approx$ 3.2 (e.g., $C_{64}H_{20}$). For the neutrals, anions, and cations listed in the figure legends, the horizontal line segments indicate the average absorption over that frequency interval, taken from theoretical calculations by Malloci et al. (2007). The thick solid line segment is the average for the six species shown.

Thus, the number of carbon atoms in a carbonaceous grain is

$$N_{\rm C} = 460\left(\frac{a}{10\ \text{Å}}\right)^3. \tag{3}$$

The smallest PAH considered in this paper has $N_{\rm C} = 20$ C atoms (corresponding to $a \approx 3.55$ Å), since smaller PAHs are photolytically unstable (Allamandola et al. 1989b). As in LD01, we assume the number of H atoms per C atom to depend on the size of the PAH:

$$\mathrm{H/C} = \begin{cases} 0.5, & N_{\rm C} \le 25, \\ 0.5(25/N_{\rm C})^{1/2}, & 25 \le N_{\rm C} \le 100, \\ 0.25, & N_{\rm C} \ge 100. \end{cases} \tag{4}$$

Figure 2 shows the adopted $C_{\rm abs}(\lambda)$ in the infrared for a PAH molecule with $\mathrm{H/C} = 5/16$ (e.g., $C_{64}H_{20}$, with $a = 5.18$ Å). Also shown are values of $C_{\rm abs}$ per C atom, averaged over wavelength intervals, for a number of molecules for which $C_{\rm abs}$ has been calculated theoretically (Malloci et al. 2007) for selected PAH molecules, cations, and anions. The first thing to note is the wide range of absorption cross sections per C. For example, in the case of the 3.3 μm C—H stretch, the integrated absorption cross section per C varies by a factor of 25 among the PAH cations. The absorption averaged over the 7.5–8.0 μm range varies by a factor of 30 among the neutral PAHs. Similar large variations in absorption cross sections are also seen at other wavelengths. Our adopted cross section falls within the range found for the sample of molecules shown in Figure 2.

Figure 3 compares our adopted absorption cross sections for both neutral and ionized PAHs.

As in LD01, as the number $N_{\rm C}$ of carbon atoms in the grain increases, we assume a continuous change in optical properties from those of PAH material when $N_{\rm C}$ is small to those of graphite when $N_{\rm C}$ is large. The transition from PAH to graphite is entirely ad hoc: we take

$$C_{\rm abs}(\lambda) = (1 - \xi_{\rm gra})C_{\rm abs}(\mathrm{PAH},\ N_{\rm C}) + \xi_{\rm gra}C_{\rm abs}(\mathrm{graphite},\ a), \tag{5}$$

where we take the graphite "weight" $\xi_{\rm gra}$ to be

$$\xi_{\rm gra} = 0.01 \tag{6}$$

for $a \le 50$ Å ($N_{\rm C} \le 5.75 \times 10^4$) and

$$\xi_{\rm gra} = 0.01 + 0.99\left[1 - \left(\frac{50\ \text{Å}}{a}\right)^3\right] \tag{7}$$

for $a \ge 50$ Å (i.e., $N_{\rm C} \ge 5.75 \times 10^4$). The rationale for this is as follows: in addition to the C—H stretching mode emission at 3.3 μm, there appears to be 2–5 μm continuum emission from the interstellar medium (ISM; Lu et al. 2003; Helou et al. 2004), and we therefore need a source of continuum opacity in the 2–5 μm region that is not provided by the C—H and C—C stretching and bending modes. Here we assume that every small PAH has a small amount of continuum opacity, equal to 1% of what would have been calculated with the optical properties of bulk graphite (i.e., $\xi_{\rm gra} = 0.01$). When the carbonaceous particles have $N_{\rm C} \gtrsim 10^5$, they are assumed to behave like bulk graphite.

Graphite is highly anisotropic, with different dielectric functions $\epsilon_\perp$ and $\epsilon_\parallel$ for electric fields perpendicular and parallel to the "*c*-axis" (the *c*-axis is normal to the "basal plane" of graphite). For 1 μm $< \lambda <$ 20 μm, absorption in small randomly oriented graphite spheres is primarily due to the free electrons in graphite moving in the basal plane. However, the basal plane conductivity is large enough that at wavelengths $\lambda > 30$ μm the absorption is primarily due to the weak but nonzero conductivity parallel to the *c*-axis. The contribution of "free electrons" to $\epsilon_\parallel$ results in an absorption peak near 30 μm (Draine & Lee 1984). This peak is seen for $a \ge 60$ Å in the right panel of Figure 3. This absorption peak results in a broad emission feature near 30 μm when the $a \gtrsim 60$ Å graphite particles are heated to $T \gtrsim 100$ K.

The peak in $C_{\rm abs}$ near 30 μm in the right panel of Figure 3 is a consequence of our adopted dielectric function for graphite, which is based on a simple free electron model that may not apply to realistic carbonaceous grains. For example, the measured absorption in amorphous carbon grains (Tanabe et al. 1983; Mennella et al. 1999) does not appear to show a peak near 30 μm. This is further discussed in § 10.7.

3. HEATING OF DUST BY STARLIGHT

We consider heating of grains by radiation with energy density per unit frequency

$$u_\nu = U u_\nu^{\rm MMP83}, \tag{8}$$

where U is a dimensionless scaling factor and $u_\nu^{\rm MMP83}$ is the interstellar radiation field (ISRF) estimated by Mathis et al. (1983) for the solar neighborhood.

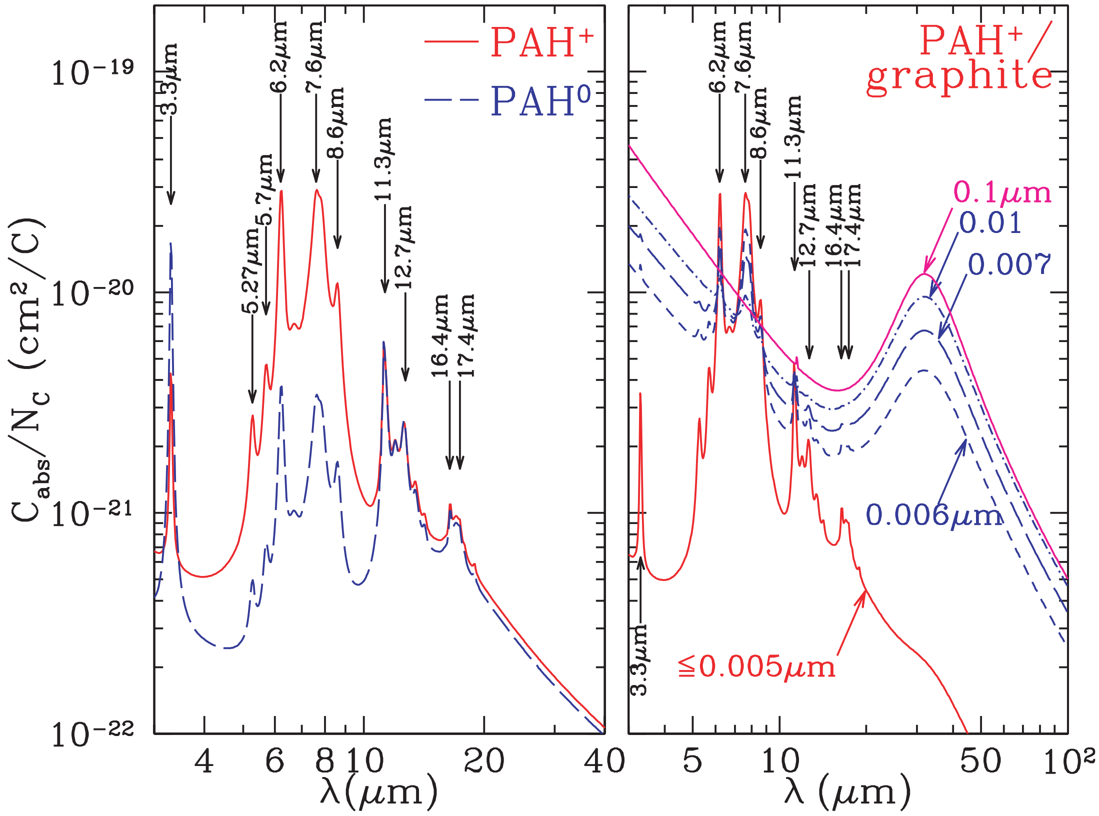

Fig. 3.—Absorption cross section per C atom for neutral and ionized PAHs (*left*) and ionized carbonaceous grains (*right*), with properties of PAHs for 6 Å < a < 50 Å and properties of graphite spheres for $a \gtrsim 100$ Å. See § 2 for details.

For each grain composition and radius a, we use a detailed model for the heat capacity (Draine & Li 2001) to calculate the function $\bar{E}(T)$, the expectation value for the vibrational energy of the grain when in equilibrium with a heat reservoir at temperature T. For a grain with vibrational energy E, the grain "temperature" $T(E)$ is taken to be the temperature at which the expectation value for the vibrational energy would be $E: \bar{E}(T) = E$; we use this temperature estimate for all values of the vibrational energy E, in this respect departing from Draine & Li (2001), who used a different estimate for the temperature when dealing with the first 20 vibrational excited states. This does not appreciably affect the emission spectrum since almost all of the absorbed photon energy is reradiated while the grain is at high temperatures.

For each grain composition, radius a, and radiation intensity scale factor U, we determine the probability distribution function dP/dT, where dP is the probability of finding the grain with temperature in $[T,\ T + dT]$. For large grains, dP/dT is approximated by a delta function $dP/dT \approx \delta(T - T_{ss})$, where the "steady state" temperature $T_{ss}(a)$ is the temperature at which the radiated power is equal to the time-averaged heating rate for a grain of radius a. For small grains, we find the steady state solution dP/dT for grains subject to stochastic heating by photon absorption and cooling by emission of infrared photons, using the "thermal-discrete" approximation (Draine & Li 2001), where the downward transition probabilities for a grain with vibrational energy E are estimated using a thermal approximation. For each grain size a and radiation intensity U, we divide the energy range $[E_{min},\ E_{max}]$ into 500 bins. E_{min} and E_{max} are found iteratively, with the requirement that the probability of the grain being outside the range $[E_{min},\ E_{max}]$ be negligible.

Figure 4 shows $dP/d\ln T$ for PAH$^+$/graphite grains for selected grain sizes, for $U = 1$ and 10^4. In Figure 4*a* one sees that small grains undergo extreme temperature excursions (the $a =$ 3.55 Å PAH occasionally reaches $T > 2000$ K), whereas larger grains (e.g., $a = 300$ Å) have temperature distribution functions that are very strongly peaked, corresponding to only small excursions around a steady state temperature T_{ss} (the temperature for which the rate of radiative cooling would equal the time-averaged rate of energy absorption).

Figure 4*b* shows $dP/d\ln T$ for $U = 10^4$. It is apparent that when the rate of starlight heating is increased, the steady state temperature approximation becomes valid for smaller grains. For example, for $U = 10^4$ one could approximate an $a = 50$ Å grain as having a steady temperature $T_{ss} \approx 150$ K, whereas for $U = 1$ the temperature excursions are very important for this grain. The radius below which single-photon heating is important, and above which the grain temperature can be approximated as being constant, is the size for which the time between photon absorptions becomes equal to the radiative cooling time (Draine & Li 2001), or (equivalently) it is the size for which the thermal energy content of the grain when at T_{ss} is equal to the energy of the most energetic photons heating the grain.

4. SINGLE-GRAIN EMISSION SPECTRA

From the probability distributions dP/dT, we calculate the time-averaged emission spectra for individual particles,

$$p_\lambda = \int 4\pi C_{abs}(\lambda) B_\lambda(T) \frac{dP}{dT}\, dT, \tag{9}$$

$$B_\lambda(T) \equiv 2hc^2 \lambda^{-5} [\exp(hc/\lambda kT) - 1]^{-1}. \tag{10}$$

Figure 5 shows the 3–30 μm emission from PAH ions and PAH neutrals heated by $U = 1$ starlight, with spectra shown for a

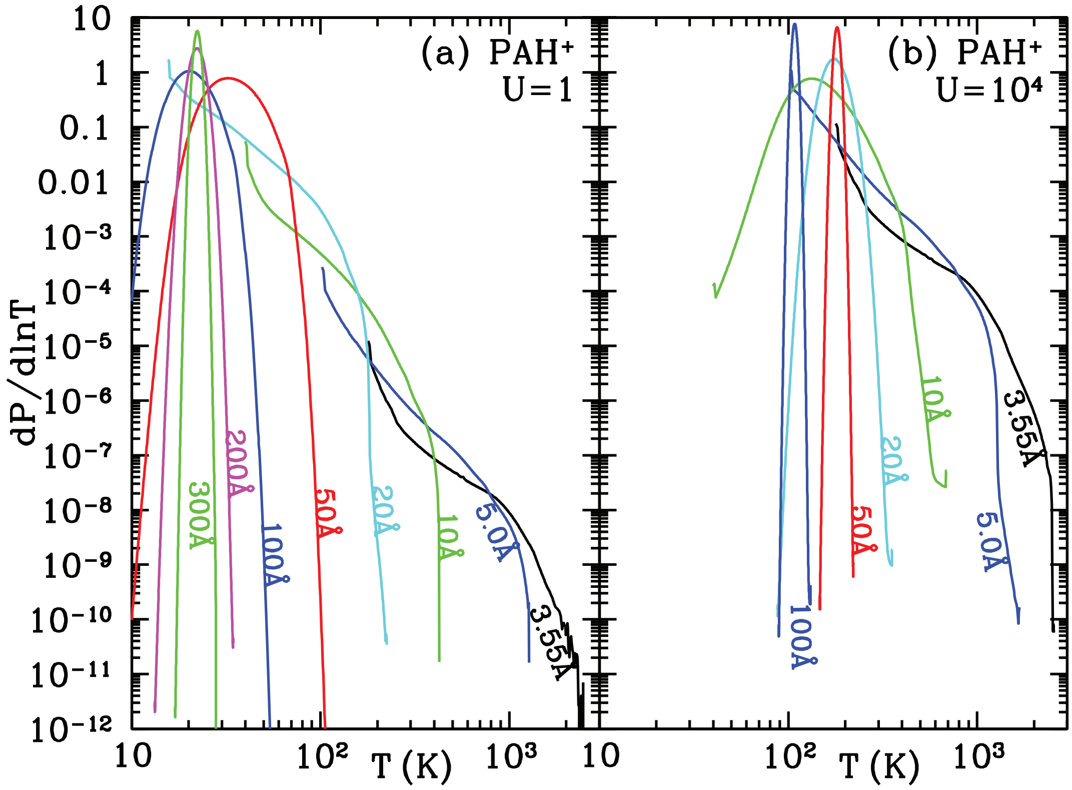

FIG. 4.—Temperature probability distribution $dP/d\ln T$ for selected carbonaceous grains heated by starlight with $U = 1$ and 10^4.

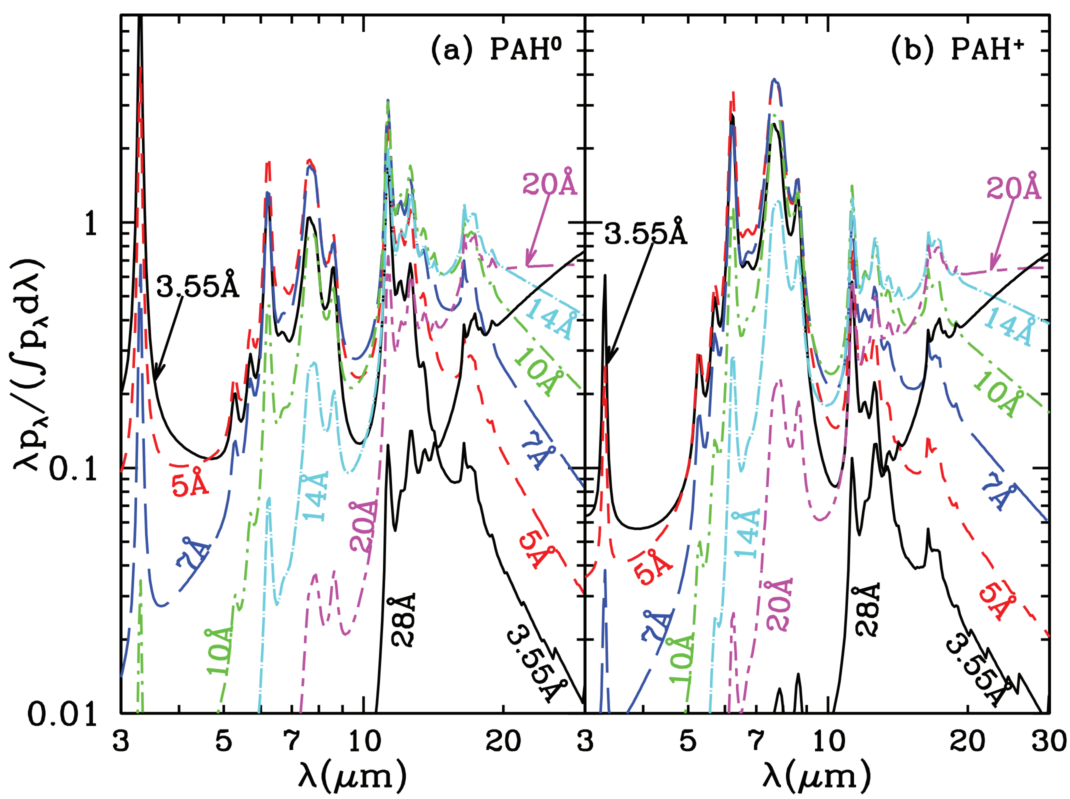

FIG. 5.—Normalized time-averaged emission spectra for $U < 10^4$ for (*a*) neutral and (*b*) ionized PAHs of various sizes (see text).

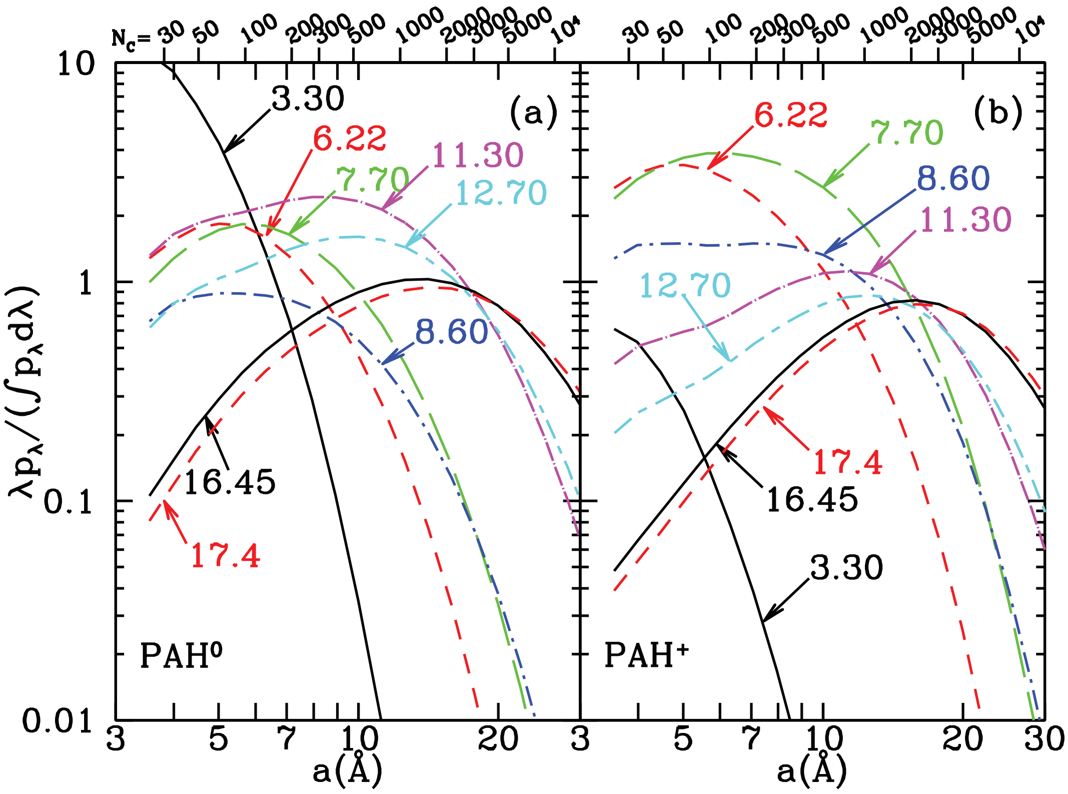

FIG. 6.—Efficiency for radiating in different emission bands, as a function of size, for ionized and neutral PAHs (see text).

number of different sizes. As expected, the short-wavelength emission (e.g., the 3.3 μm feature) is strong only for the smallest particles, which can be heated to $T \gtrsim 10^3$ K by absorption of a single ultraviolet photon (see Fig. 4). As the particle size becomes larger, the short-wavelength emission falls off, and an increasing fraction of the absorbed starlight energy is radiated in the longer wavelength modes. Emission in the 17 μm complex, for example, is most efficient for $a \approx 15$ Å.

The dependence of the feature emission on grain size is shown in Figure 6. From this plot it is apparent that emission in the 3.30 μm feature will be almost entirely due to $a \lesssim 6$ Å, or $N_C \lesssim 10^2$, whereas grains with radii as large as 12 Å, or $N_C \approx 10^3$, are efficient at converting absorbed starlight into 7.7 μm emission. The 11.3 μm feature can be produced by particles as large as $a \approx 20$ Å or $N_C \approx 4000$, and the 16.45 μm feature and 17.4 μm complex are efficiently produced by PAH particles in the 8–25 Å size range ($300 \lesssim N_C \lesssim 10^4$).

The PAH emission spectra shown in Figure 5 and the band emission efficiencies shown in Figure 6 are independent of the starlight intensity U in the single-photon heating regime, $U \lesssim 10^4$ for $\lambda \lesssim 30$ μm. For larger grains, and at higher starlight intensities, the emission spectra do depend on U. If $C_{abs} \propto \lambda^{-2}$ for $\lambda \gtrsim 30$ μm, then the power radiated by the grain $\propto T^6$, the steady state temperature $T_{ss} \propto U^{1/6}$, and the infrared emission will peak at a wavelength $\lambda_p \propto 1/T_{ss} \propto U^{-1/6}$.

The PAHs in the ISM will consist of a mixture of neutral and ionized particles. For a given size PAH, the ionization balance will depend on the gas temperature, the electron density, and the ultraviolet radiation field (Weingartner & Draine 2001b). Here we adopt the ionization balance estimated by LD01 for the diffuse ISM in the Milky Way: a weighted sum of the ionization fractions calculated for PAHs in the cold neutral medium (CNM), warm neutral medium (WNM), and warm ionized medium (WIM). For this weighted sum of neutral and ionized PAHs, $\lambda p_\lambda/p$ at selected wavelengths is shown as a function of grain size in Figure 7. Note that most of the selected wavelengths coincide with the positions of PAH emission features, thus indicating how PAH size affects the efficiency of converting starlight energy into IR emission features. The adopted ionization fraction as a function of grain size is shown in Figure 8.

Figure 7 also shows $\lambda p_\lambda/p$ evaluated at the 23.7 μm wavelength of the MIPS 24 μm band. We see that PAHs in the 15–40 Å size range ($2000 \lesssim N_C \lesssim 3 \times 10^4$) are relatively efficient at converting starlight energy into 24 μm continuum following single-photon heating (Fig. 4 shows that a single $h\nu < 13.6$ eV photon can heat a 20 Å PAH to $\sim$170 K). The term "very small grains" is sometimes used to describe small grains that contribute continuum emission into the *IRAS* 25 μm band or the MIPS 24 μm band: here we see that such grains must have effective radii in the 15–40 Å range to efficiently convert absorbed stellar energy into $\sim$24 μm continuum emission.

Figures 9 and 10 show 2–200 μm emission spectra calculated for carbonaceous grains and amorphous silicate grains with sizes extending from $a = 3.55$ to 5000 Å. As expected, the emission from $a \gtrsim 60$ Å grains peaks at $\lambda \approx 100U^{-1/6}$ μm. However, for $U = 10^6$ and 10^7, λp_λ for $a \gtrsim 60$ Å carbonaceous grains has two peaks: one near the peak in λB_λ near $100U^{-1/6}$ μm, and the second near 30 μm, the latter resulting from the peak in $C_{abs}(\lambda)$ near 30 μm (see Fig. 3*b*). As discussed in § 2, the 30 μm opacity peak in the present model produced by graphite in the present model may not apply to the carbonaceous material in interstellar dust.

5. DUST MIXTURES

Interstellar dust in the Milky Way and other galaxies includes a wide range of grain sizes. Here we consider the size distributions

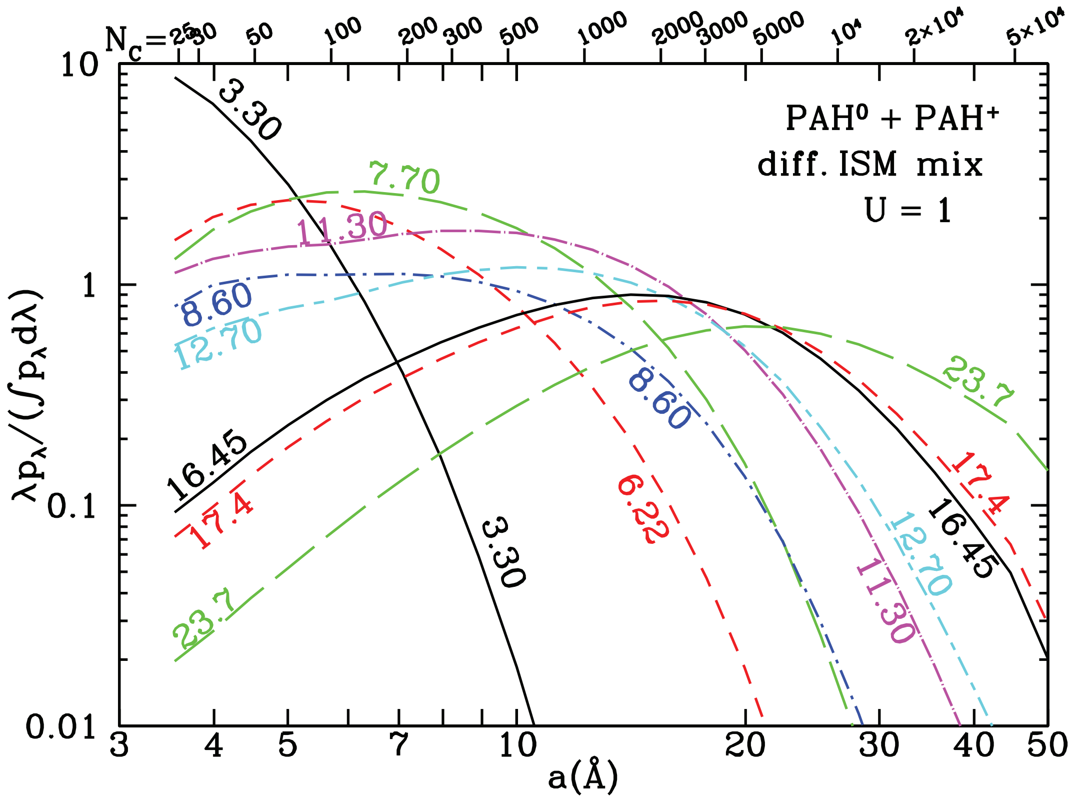

FIG. 7.—Parameter λp_λ divided by the total time-averaged power p radiated by the grain, as a function of grain size a, for selected values of wavelength λ; curves are labeled by the value of $\lambda(\mu m)$. We assume a mix of neutral and ionized PAHs, with ionization fraction as in Fig. 8. The effective wavelength of the MIPS 24 μm; band is 23.7 μm; the other wavelengths are at peaks of emission features.

put forward by WD01 to reproduce the wavelength-dependent extinction on Milky Way sight lines with extinction curves characterized by $R_V \equiv A_V/(A_B - A_V) = 3.1$. WD01 included a population of small ($a \lesssim 50$ Å) carbonaceous particles with specified total mass. LD01 showed that if these small carbonaceous particles had the physical properties of PAHs and were distributed in two log-normal components,

$$\frac{dn}{da} = \sum_{j=1}^{2} \frac{n_{0j}}{a} \exp\left\{ -\frac{\left[\ln\left(a/a_{0j}\right)\right]^2}{2\sigma_j^2} \right\} + \text{nonlognormal contribution}, \tag{11}$$

the resulting infrared emission was approximately consistent with the diffuse emission observed by IRTS (Onaka et al. 1996; Tanaka et al. 1996). The nonlognormal contribution to equation (11) is given by equation (4) of WD01, with parameter values taken from that paper except for a reduction in the numbers of grains per H by a factor of 0.92, as recommended by Draine (2003). Note that the nonlognormal term also extends continuously down to the smallest sizes.

We continue to use equation (11) for dn/da, but we have modified the values of the parameters a_{0j} and σ_j, as given in Table 2. The factors n_{0j} in equation (11) are related to the numbers b_j of carbon atoms per total H in each of the lognormal components:

$$n_{0j} = \frac{3}{(2\pi)^{3/2}} \frac{\exp\left(4.5\sigma_j^2\right)}{1 + \text{erf}\left(x_j\right)} \frac{m_C}{\rho_C a_{Mj}^3 \sigma_j} b_j, \tag{12}$$

$$x_j = \frac{\ln\left(a_{Mj}/a_{\min}\right)}{\sigma_j\sqrt{2}}, \tag{13}$$

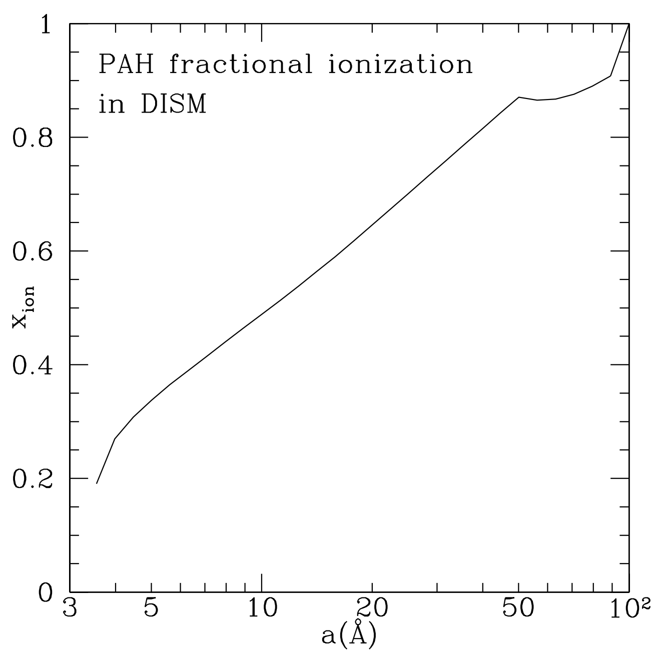

FIG. 8.—Adopted fractional ionization in diffuse ISM (LD01).

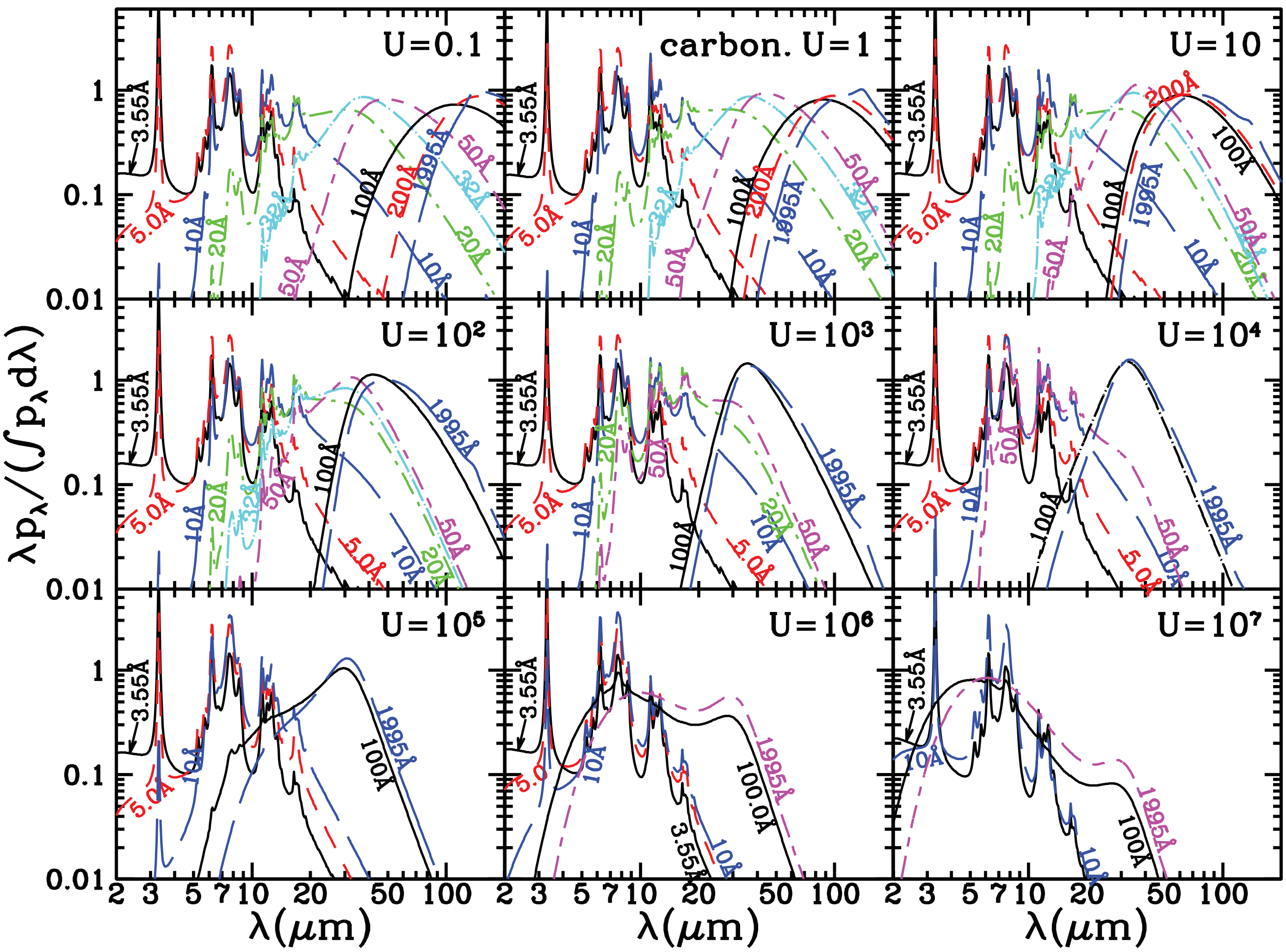

FIG. 9.—Emission for selected sizes of carbonaceous grains for $U = 0.1$–10^7. For $a < 100$ Å PAHs are assumed to have $x_{\rm ion}$ from Fig. 8 (see text).

where $\rho_{\rm C}$ is the carbon mass density, $m_{\rm C}$ is the mass of a carbon atom, and

$$a_{Mj} \equiv a_{0j} \exp\left(3\sigma_j^2\right) \tag{14}$$

is the location of the peak in the mass distribution $\propto a^3 dn/d \ln a$. Note that the nonlognormal term in equation (11) also contributes to the population of $N_{\rm C} < 10^3$ PAHs.

These size distributions have been constructed for various amounts of carbonaceous material in the very small PAH particles. The size distributions all reproduce the observed wavelength-dependent extinction in the Milky Way, for sight lines with $R_V \equiv A_V/E(B-V) \approx 3.1$. Because the abundance of ultrasmall grains is important for the infrared emission, as well as other applications, Table 3 gives the amount of carbon present in grains containing $<10^2$, <200, <500, $<10^3$, $<10^4$, and $<10^5$ C atoms, for the seven different grains models. Models $j_M = 1$–7 have $(b_1 + b_2) = 0.92 \times 60 \times 10^{-6}[(j_M - 1)/6]$. The mass distributions for carbonaceous grains are shown in Figure 11. (The silicate mass distribution is shown in Fig. 2 of WD01, except that the dust abundances should be multiplied by 0.92.)

The emissivity per H nucleon for a dust mixture heated by starlight intensity U is

$$j_\nu(U) = \sum_j \int da \frac{dn_j}{da} \int C_{\rm abs}(j, a, \nu) B_\nu(T) \left(\frac{dP}{dT}\right)_{j,a,U} dT, \tag{15}$$

$$B_\nu(T) \equiv \frac{2h\nu^3}{c^2} \frac{1}{\exp(h\nu/kT) - 1}, \tag{16}$$

where the sum is over compositions j and the temperature distribution function dP/dT depends on composition j, radius a, and starlight intensity U.

Taking dP/dT calculated for the local starlight intensity $U = 1$, summing over the grain size distribution and over the fractional ionization shown in Figure 8, we obtain the emission per H nucleon j_λ shown in Figure 12. The emission at $\lambda < 20$ μm depends strongly on the PAH abundance $q_{\rm PAH}$.

Figure 13 shows the emission calculated for the model with $q_{\rm PAH} = 4.6\%$, but for different starlight intensities U. For $U \lesssim 10^3$, the normalized emission at $\lambda < 20$ μm is essentially independent of U because the emission is almost exclusively the result of single-photon heating, with the PAH particles cooling off almost completely between photon absorptions. This remarkable

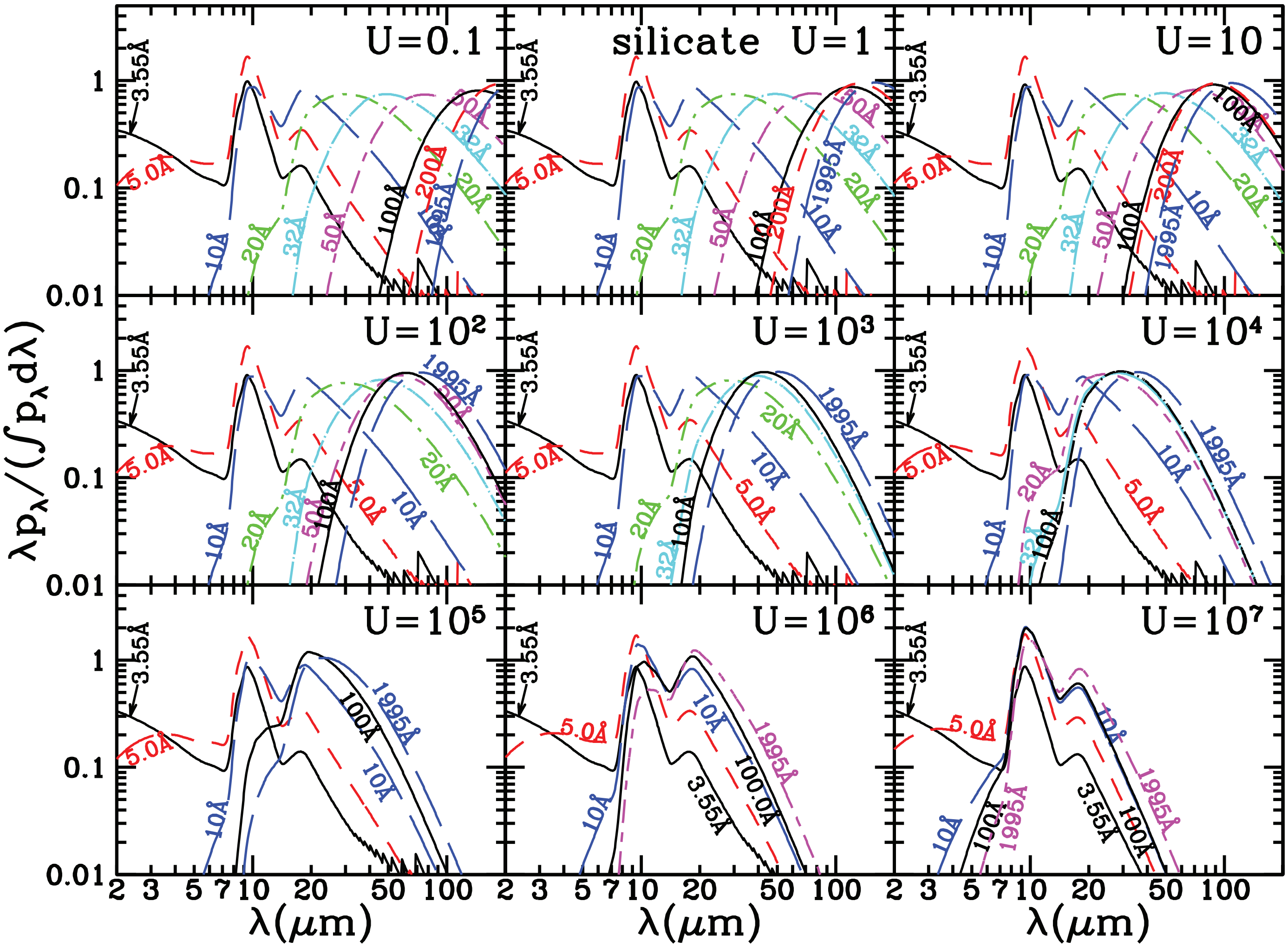

Fig. 10.—Emission for amorphous silicate grains of various sizes for $U = 0.1$–10^7 (see text).

invariance of the PAH emission spectra over order-of-magnitude variations in starlight intensities has been observed in a wide range of environments (see, e.g., Boulanger et al. 2000; Kahanpää et al. 2003; Sakon et al. 2004). For $U \gtrsim 10^4$, however, the mean time between photon absorptions becomes shorter than the radiative cooling time for a PAH with $\sim$1 eV of internal energy, so that the small grains do not cool completely between photon absorptions. Photon absorptions are then able to take them to higher peak temperatures, and the fraction of the power radiated at $\lambda < 20$ μm increases with increasing U.

6. FIR AND SUBMILLIMETER EMISSION

The focus in the present dust model has been on the PAH features, but the model is intended to reproduce the thermal dust emission at FIR and submillimeter wavelengths as well. The opacities of the amorphous silicate and graphite particles in the model are calculated using dielectric functions. The graphite dielectric function is based on laboratory measurements of graphite. Because the nature of interstellar amorphous silicate material is uncertain, the FIR and submillimeter behavior is not constrained by laboratory data. Draine & Lee (1984) made an estimate of the imaginary part of the dielectric function of interstellar amorphous silicate.

Finkbeiner et al. (1999, hereafter FDS99) used *COBE* FIRAS observations of the sky at high Galactic latitudes, after removal of the cosmic background radiation and zodiacal emission, to characterize the emission from diffuse gas and dust in the Milky Way. They excluded $|b| < 7°$, the Magellanic Clouds, H II regions in Orion and Ophiuchus, and an additional 16.3% of the sky where the data were of lower quality. The final data set comprises 81% of the $|b| > 7°$ sky. For this region, FDS99 find an empirical fit that quite accurately reproduces the observed 100 μm–3 mm spectra, using two parameters for each pixel: the 100 μm intensity I_{ν_0} and a temperature T_2 that determines the shape of the $\lambda >$ 100 μm spectrum:

$$I_\nu = I_{\nu_0} \frac{(\nu/\nu_0)^{2.70} B_\nu(T_2) + 0.515(\nu/\nu_0)^{1.67} B_\nu(T_1)}{B_{\nu_0}(T_2) + 0.515 B_{\nu_0}(T_1)},$$

$$T_1 = 9.4\ \mathrm{K} \left(\frac{T_2}{16.2\ \mathrm{K}}\right)^{1.182}, \qquad (17)$$

TABLE 2
PAH Size Distribution Parameters

Parameter	LD01	This Paper
$b_1/(b_1+b_2)$	0.75	0.75
$b_2/(b_1+b_2)$	0.25	0.25
a_{01} (Å)	3.5	4.0
a_{02} (Å)	30.	20.
σ_1	0.4	0.4
σ_2	0.4	0.55

TABLE 3
Physical Dust Models

j_M	Model	q_{PAH} (%)	M_{dust}/M_H [a]	C/H (ppm) in PAHs $N_C < 100$	$N_C < 200$	$N_C < 500$	$N_C < 10^3$	$N_C < 10^4$	$N_C < 10^5$
1	MW3.1_00	0.47	0.0100	1.2	1.8	2.9	3.9	8.7	17.0
2	MW3.1_10	1.12	0.0100	3.5	5.6	8.0	9.4	13.6	21.5
3	MW3.1_20	1.77	0.0101	5.8	9.4	13.2	14.9	18.6	26.0
4	MW3.1_30	2.50	0.0102	8.3	13.4	18.6	20.8	24.2	31.1
5	MW3.1_40	3.19	0.0102	10.9	17.6	24.4	27.1	30.7	37.9
6	MW3.1_50	3.90	0.0103	13.5	21.8	30.2	33.4	37.1	44.4
7	MW3.1_60	4.58	0.0104	16.1	26.1	36.1	39.8	43.9	51.6
8	LMC2_00	0.75	0.00343	0.9	1.2	1.8	2.2	3.5	5.0
9	LMC2_05	1.49	0.00344	1.6	2.6	3.7	4.3	5.2	6.7
10	LMC2_10	2.37	0.00359	2.6	4.4	6.3	7.1	7.9	9.6
11	SMC	0.10	0.00206	0.1	0.1	0.2	0.3	0.4	0.5

[a] $M_{dust}/M_{gas} = (1/1.36)(M_{dust}/M_H)$.

where $\nu_0 = c/100\ \mu m = 3000$ GHz. The mean value $\langle T_2 \rangle = 16.2$ K. Variations in T_2 are presumably the result of variations in the intensity of the starlight heating the grains; a simple model suggests

$$T_2 = (16.2\ \mathrm{K}) U_{FDS}^{1/6.70}, \quad T_1 = (9.4\ \mathrm{K}) U_{FDS}^{1/5.67}, \qquad (18)$$

where U_{FDS} is the intensity of the starlight heating the dust, relative to the average for the region analyzed by FDS99.

Based on the observed spectrum of equation (17) with $T_2 = 16.2$ K, LD01 made small adjustments to the imaginary part of the dielectric function for the amorphous silicate material at $\lambda > 250\ \mu m$ to improve agreement with the observed emission spectrum. The real part of the dielectric function is obtained from the imaginary part using the Kramers-Kronig relations (Draine & Lee 1984). The resulting dielectric function is used to calculate absorption cross sections for amorphous silicate spheres in the present work.

Figure 14*a* shows the observed FIR and submillimeter emission spectrum, as given by equation (17) with $T_2 = 16.2$ K (i.e., $U_{FDS} = 1$). Also shown are emission spectra calculated for the present model for two values of the starlight intensity: $U = 0.8$ and 1. Both spectra have shapes that are close to the observed spectrum, but the $U = 0.8$ spectrum agrees to within a few percent from 100 μm to 1.5 mm. Evidently $U_{FDS} \approx 1.2U$ gives the correspondence between the starlight intensity U in the present model (normalized to the estimate of the local interstellar radiation field by Mathis et al. 1983) and the starlight intensity U_{FDS} relative to the "average" for the 71% of the sky analyzed by FDS99.

Figure 14*b* shows the emission spectra for the model when the radiation field is lowered to $U = 0.5$ and raised to $U = 2$; these spectra compare well with the FDS99 spectra for $U_{FDS} = 0.6$ and 2.4, as expected from the correspondence $U_{FDS} \approx 1.2U$ inferred from Figure 14*a*.

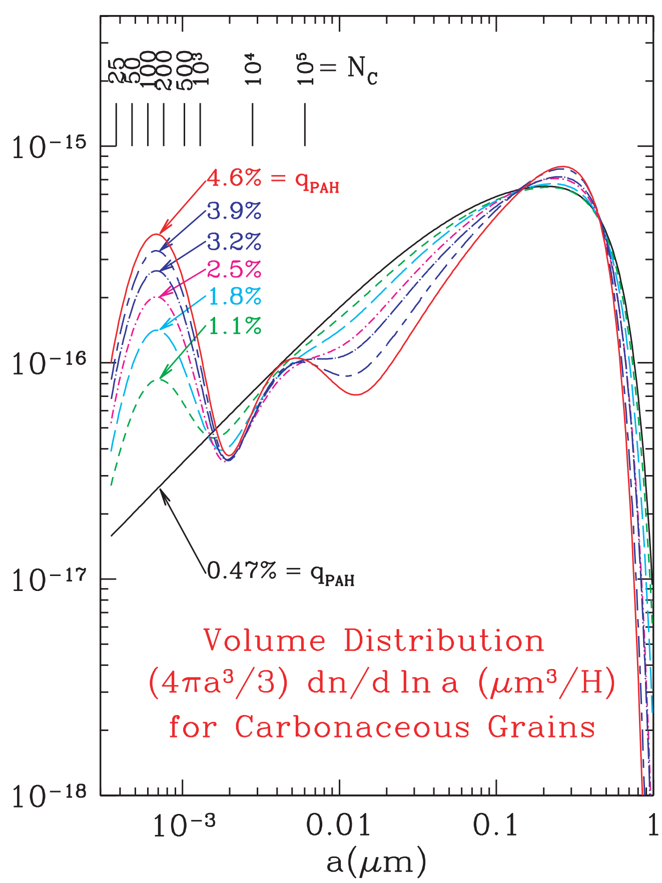

Fig. 11.—Size distributions $j_M = 1$–7 for carbonaceous grains. Mass distributions of silicate grains are given by Fig. 2 of WD01 multiplied by 0.92 (see text).

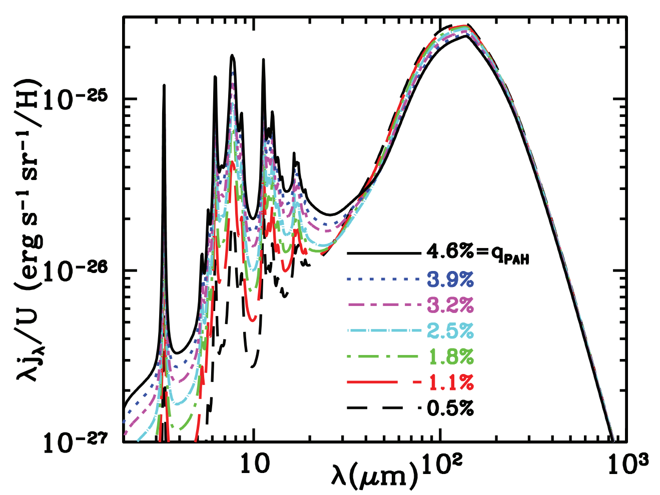

Fig. 12.—Emission spectra for Milky Way dust models with various q_{PAH} (dust models $j_M = 1$–7), heated by starlight with $U = 1$. Tabulated spectra for this and other cases are available online at http://www.astro.princeton.edu/~draine/dust/irem.html.

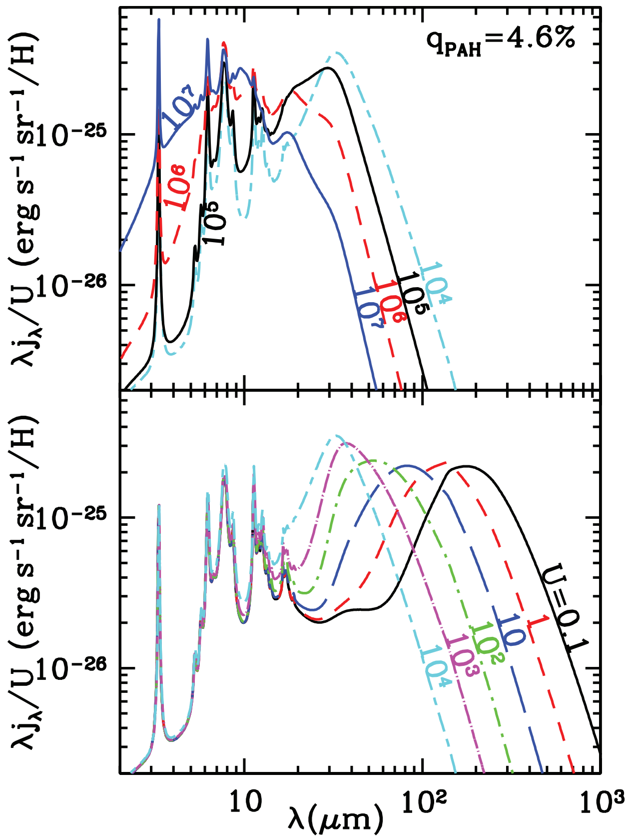

FIG. 13.—Emission spectra for size distribution $j_M = 7$ for selected starlight intensity scale factors U.

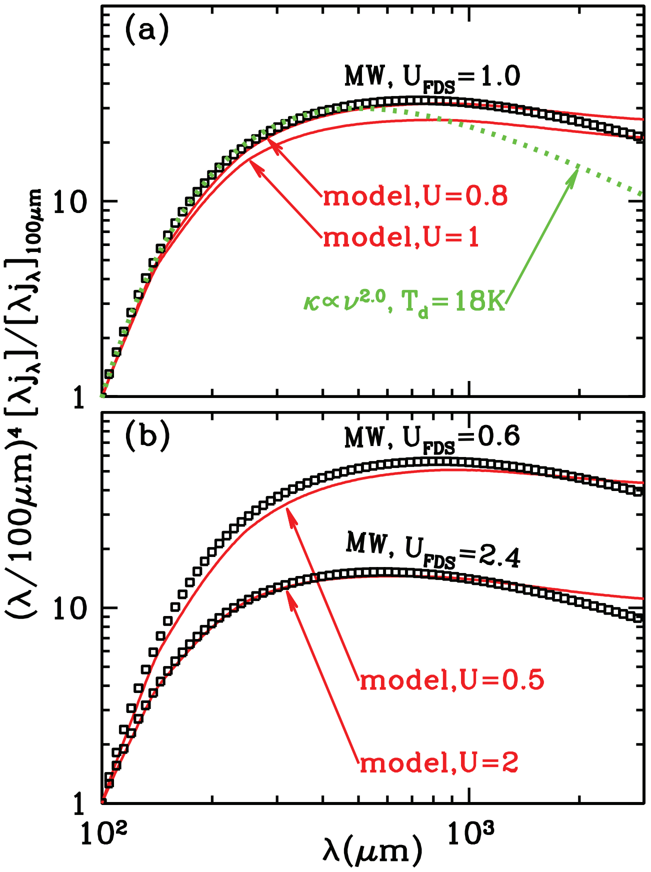

FIG. 14.—(*a*) *Squares*: Observed spectrum, relative to the 100 μm emission, of Milky Way dust from FDS99 given by eqs. (17) and (18) with $T_2 = 16.2$ K. *Solid curve*: 100 μm–3 mm emission spectrum for MW dust model with $q_{\rm PAH} = 4.6\%$, for $U = 0.8$ and 1. The $U = 0.8$ model approximately reproduces the observed emission for $T_2 = 16.2$ K, although having excess emission at $\lambda > 1.5$ mm. The good agreement between the $U = 0.8$ model and the observed spectrum with $U_{\rm FDS} = 1$ suggests a correspondence $U_{\rm FDS} \approx 1.2U$. *Dotted curve*: Single-temperature dust model with opacity $\kappa \propto \nu^2$ and $T = 18$ K, for comparison. A single modified blackbody produces insufficient emission for $\lambda \gtrsim 500$ μm. (*b*) Observed spectra for $U_{\rm FDS} = 0.6$ and 2.4 (*squares*) and the present dust model for $U = 0.5$ and 2 (*solid curves*).

We conclude that the present dust model can successfully reproduce the emission observed from dust in the diffuse ISM of the Milky Way (including dust in molecular clouds at $|b| > 7°$ and away from Orion and Ophiuchus) out to wavelengths as long as 2 mm without introduction of additional emission components.

7. *SPITZER* IRAC AND MIPS BAND RATIOS

For interpreting observations with the IRAC and MIPS cameras on *Spitzer*, the quantities of interest are the band-convolved emissivities and luminosities

$$\langle j_\nu \rangle_{\rm band} \equiv \frac{\int R_{\rm band}(\nu) j_\nu\, d\nu}{\int (\nu/\nu_{\rm band})^\beta R_{\rm band}(\nu)\, d\nu},$$

$$\langle L_\nu \rangle_{\rm band} \equiv \frac{\int R_{\rm band}(\nu) L_\nu\, d\nu}{\int (\nu/\nu_{\rm band})^\beta R_{\rm band}(\nu)\, d\nu}, \qquad (19)$$

$$\langle \nu j_\nu \rangle_{\rm band} \equiv \nu_{\rm band} \langle j_\nu \rangle_{\rm band}, \quad \langle \nu L_\nu \rangle_{\rm band} \equiv \nu_{\rm band} \langle L_\nu \rangle_{\rm band}, \qquad (20)$$

where $R_{\rm band}(\nu)$ is the relative response per unit power for the combination of optics, filter, and detector and $\nu_{\rm band} \equiv c/\lambda_{\rm band}$, with $\lambda_{\rm band}$, the nominal wavelength of the band, given in Table 4.

Table 4 gives $\langle \nu j_\nu \rangle_{\rm band}$ for the four IRAC bands,[6] the two "peakup" bands of the Infrared Spectrograph (IRS),[7] and the three MIPS bands.[8] Table 5 gives emissivities convolved with photometric bands of the *AKARI* satellite (Kawada et al. 2004; Onaka et al. 2004) and model emissivities convolved with the three bands of the *Herschel* PACS instrument,[9] and the three bands of the *Herschel* SPIRE instrument[10] are given in Table 6. Emissivities $\langle \nu j_\nu \rangle_{\rm band}$ are given for selected grain models with several different values of $q_{\rm PAH}$ and for different values of the starlight intensity scale factor U.

Figure 15 shows $\langle \nu L_\nu \rangle_{\rm band}$ relative to the total infrared (TIR) dust luminosity

$$L_{\rm TIR} \equiv \int_0^\infty L_\nu\, d\nu \qquad (21)$$

for five bands: IRAC 3.6 μm, IRAC 7.9 μm, MIPS 24 μm, MIPS 71 μm, and MIPS 160 μm. Results are given for grain models

[6] $R_{\rm band}(\nu) \propto (1/h\nu)S_{\rm band}(\nu)$, where the relative response per photon $S_{\rm band}(\nu)$ is obtained from http://ssc.spitzer.caltech.edu/irac/spectral_response.html. The IRAC calibration uses $\beta = -1$.

[7] $R_{\rm band}(\nu) \propto (1/h\nu)S_{\rm band}(\nu)$, where the relative quantum efficiency $S_{\rm band}(\nu)$ is given in Fig. 6.1 of the Infrared Spectrograph Data Handbook, ver. 2.0. The IRS peakup calibration uses $\beta = -1$.

[8] $R_{\rm band}(\nu)$ is obtained from http://ssc.spitzer.caltech.edu/mips/spectral_response.html. The MIPS calibration is for a 10^4 K blackbody, i.e., $\beta = 2$.

[9] A. Poglitsch has kindly provided provisional $R_{\rm band}(\nu)$ for PACS. The calibration procedures for PACS have not yet been finalized. Here we assume $\beta = 2$.

[10] M. Griffin has kindly provided provisional $R_{\rm band}(\nu)$ for SPIRE. The calibration procedures for SPIRE have not yet been finalized. Here we assume $\beta = 2$.

TABLE 4
Model Emissivities $\langle \nu j_\nu \rangle_{\rm band}$ (ergs s^{-1} sr^{-1} H^{-1})[a] for *Spitzer Space Telescope*

U	$q_{\rm PAH}$ (%)	IRAC 1 3.550 μm	IRAC 2 4.493 μm	IRAC 3 5.731 μm	IRAC 4 7.872 μm	IRS PU1 16 μm	IRS PU2 22 μm	MIPS 1 23.68 μm	MIPS 2 71.42 μm	MIPS 3 155.9 μm
0.5	0.47	5.66E−28	1.54E−28	1.31E−27	4.05E−27	4.86E−27	5.91E−27	5.83E−27	5.04E−26	1.25E−25
	1.12	1.55E−27	4.30E−28	3.53E−27	9.17E−27	6.41E−27	6.27E−27	6.05E−27	4.76E−26	1.21E−25
	1.77	2.56E−27	7.09E−28	5.77E−27	1.43E−26	7.97E−27	6.62E−27	6.26E−27	4.54E−26	1.19E−25
	3.19	4.78E−27	1.34E−27	1.07E−26	2.60E−26	1.24E−26	8.87E−27	8.16E−27	4.11E−26	1.12E−25
	4.58	7.07E−27	1.98E−27	1.58E−26	3.81E−26	1.73E−26	1.14E−26	1.04E−26	3.66E−26	1.05E−25
1.0	0.47	1.13E−27	3.08E−28	2.63E−27	8.10E−27	9.84E−27	1.21E−26	1.20E−26	1.35E−25	2.27E−25
	1.12	3.11E−27	8.59E−28	7.06E−27	1.84E−26	1.29E−26	1.29E−26	1.24E−26	1.28E−25	2.21E−25
	1.77	5.11E−27	1.42E−27	1.15E−26	2.87E−26	1.60E−26	1.35E−26	1.28E−26	1.22E−25	2.18E−25
	3.19	9.55E−27	2.68E−27	2.14E−26	5.20E−26	2.50E−26	1.80E−26	1.66E−26	1.11E−25	2.06E−25
	4.58	1.41E−26	3.96E−27	3.15E−26	7.62E−26	3.47E−26	2.32E−26	2.11E−26	9.89E−26	1.94E−25
3.0	0.47	3.39E−27	9.24E−28	7.90E−27	2.44E−26	3.07E−26	3.95E−26	3.92E−26	5.80E−25	5.19E−25
	1.12	9.32E−27	2.58E−27	2.12E−26	5.51E−26	3.99E−26	4.14E−26	4.03E−26	5.53E−25	5.06E−25
	1.77	1.53E−26	4.25E−27	3.47E−26	8.62E−26	4.91E−26	4.32E−26	4.12E−26	5.35E−25	5.01E−25
	3.19	2.86E−26	8.05E−27	6.41E−26	1.56E−25	7.58E−26	5.66E−26	5.25E−26	4.89E−25	4.77E−25
	4.58	4.24E−26	1.19E−26	9.46E−26	2.29E−25	1.05E−25	7.22E−26	6.60E−26	4.41E−25	4.57E−25
5.0	0.47	5.66E−27	1.54E−27	1.32E−26	4.07E−26	5.28E−26	6.97E−26	6.95E−26	1.08E−24	7.30E−25
	1.12	1.55E−26	4.29E−27	3.53E−26	9.19E−26	6.80E−26	7.27E−26	7.10E−26	1.03E−24	7.13E−25
	1.77	2.56E−26	7.08E−27	5.78E−26	1.44E−25	8.32E−26	7.54E−26	7.23E−26	1.00E−24	7.06E−25
	3.19	4.77E−26	1.34E−26	1.07E−25	2.60E−25	1.28E−25	9.76E−26	9.10E−26	9.20E−25	6.76E−25
	4.58	7.06E−26	1.98E−26	1.58E−25	3.81E−25	1.77E−25	1.24E−25	1.14E−25	8.36E−25	6.50E−25
10.0	0.47	1.13E−26	3.08E−27	2.63E−26	8.17E−26	1.12E−25	1.54E−25	1.54E−25	2.37E−24	1.13E−24
	1.12	3.11E−26	8.59E−27	7.07E−26	1.84E−25	1.42E−25	1.59E−25	1.56E−25	2.27E−24	1.11E−24
	1.77	5.11E−26	1.42E−26	1.15E−25	2.88E−25	1.72E−25	1.63E−25	1.57E−25	2.21E−24	1.10E−24
	3.19	9.55E−26	2.68E−26	2.14E−25	5.21E−25	2.61E−25	2.07E−25	1.94E−25	2.05E−24	1.06E−24
	4.58	1.41E−25	3.96E−26	3.15E−25	7.63E−25	3.59E−25	2.59E−25	2.39E−25	1.88E−24	1.02E−24
100.0	0.47	1.13E−25	3.09E−26	2.67E−25	8.67E−25	1.68E−24	2.80E−24	2.89E−24	2.16E−23	3.72E−24
	1.12	3.11E−25	8.62E−26	7.12E−25	1.89E−24	1.94E−24	2.78E−24	2.83E−24	2.09E−23	3.66E−24
	1.77	5.12E−25	1.42E−25	1.16E−24	2.93E−24	2.20E−24	2.75E−24	2.77E−24	2.06E−23	3.64E−24
	3.19	9.57E−25	2.69E−25	2.15E−24	5.26E−24	3.07E−24	3.09E−24	3.03E−24	1.95E−23	3.55E−24
	4.58	1.41E−24	3.97E−25	3.17E−24	7.70E−24	4.07E−24	3.56E−24	3.41E−24	1.85E−23	3.48E−24

[a] Additional models, with spectra, are available online at http://www.astro.princeton.edu/~draine/dust/irem.html.

$j_M = 1$–7, with the model results labeled by the value of $q_{\rm PAH}$. As expected, the 3.6 and 7.9 μm emission per unit total power is entirely the result of single-photon heating at low values of U, and therefore $\langle \nu L_\nu \rangle_{7.9}/L_{\rm TIR}$ is independent of U for $U \lesssim 10^3$ and $\langle \nu L_\nu \rangle_{3.6}/L_{\rm TIR}$ is independent of U for $U \lesssim 10^5$. In addition, $\langle \nu L_\nu \rangle_{3.6}/L_{\rm TIR}$ and $\langle \nu L_\nu \rangle_{7.9}/L_{\rm TIR}$ are both approximately proportional to $q_{\rm PAH}$ in the low-U limit, as expected. For small values of U, the 24 μm emission is also the result of single-photon heating, and $\langle \nu L_\nu \rangle_{24}/L_{\rm TIR}$ is independent of U for $U \lesssim 10$.

Flagey et al. (2006) extracted the diffuse ISM emission from IRAC imaging of various regions of the Milky Way obtained by the Galactic First Look Survey (GFLS) and the Galactic Legacy Infrared Midplane Survey Extraordinaire (GLIMPSE). The model emission spectra, convolved with the response function for the IRAC bands, can be compared to the observed colors of the diffuse emission.

Figure 16*a* shows the colors of the observed emission in the IRAC 3.6, 5.7, and 7.9 μm bands. The filled square shows the color calculated for the present dust model with the value of $q_{\rm PAH} \approx 4.6\%$ that appears to be applicable to the dust in the Milky Way and other spiral galaxies with near-solar metallicity (Draine et al. 2007). The model with $q_{\rm PAH} \approx 4.6\%$ appears to be in good agreement with the Milky Way observations in Figure 16*a*. First of all, $\langle \nu F_\nu \rangle_{5.7}/\langle \nu F_\nu \rangle_{7.9}$ is within the range of observed values, indicating that the adopted $C_{\rm abs}(\lambda)$ has approximately the correct shape over the 5.5–8.5 μm wavelength range. Second, the ratio of 3.6 μm emission divided by 7.9 μm emission is close to the observed value. The emission into the IRAC 3.6 μm band is sensitive to the abundances of the very smallest PAHs, with $N_{\rm C} \lesssim 75$ (see Fig. 6); we can therefore conclude that the size distribution adopted by the present model has approximately the correct amount of PAH mass in the interval $20 \lesssim N_{\rm C} \lesssim 75$, at least relative to the PAH mass in the interval $20 \lesssim N_{\rm C} \lesssim 10^3$ that radiates efficiently into the IRAC 8 μm band. The ratio of the 3.6 μm emission to the 8 μm emission of course is sensitive to the assumed PAH charge state (see Fig. 6). The present model assumes a mixture of ionization conditions that is intended to be representative of the local ISM (see Fig. 8). If the actual ionized fraction for the PAHs is higher than in our model, then the actual mass fraction in the interval $20 \lesssim N_{\rm C} \lesssim 75$ would have to be even higher than the adopted size distribution (shown in Fig. 11). Conversely, if the PAH neutral fraction is actually higher than in our model, then the PAH mass fraction in the $20 \lesssim N_{\rm C} \lesssim 75$ range could be reduced.

Observations of external galaxies by *ISO* and *Spitzer* have been interpreted as showing diffuse nonstellar emission in the 2.5–5 μm wavelength range (Lu et al. 2003; Helou et al. 2004), consistent with thermal emission from dust with $Q_{\rm abs} \propto \nu^2$ and temperatures in the ~750–1000 K range. The GFLS and GLIMPSE images also appear to contain diffuse emission in the 4.5 μm band (Flagey et al. 2006). Figure 16*b* shows the observed ratio of 4.5 μm emission relative to 7.9 μm emission, as well as the model values. The observed 4.5 μm emission is perhaps 50% stronger (relative to the 8.0 μm emission) than the models.

In many cases it is desirable to try to estimate the total infrared luminosity from the observed fluxes in the IRAC and MIPS bands.

TABLE 5
Model Emissivities $\langle \nu j_\nu \rangle_{\rm band}$ (ergs s^{-1} sr^{-1} H^{-1})[a] for Akari

U	$q_{\rm PAH}$ (%)	N3 3.2 μm	N4 4.1 μm	S7 7.0 μm	S9W 9.0 μm	S11 11.0 μm	L15 15 μm	L18W 18 μm	L24 24 μm	N60 65 μm	WIDE-S 80. μm	WIDE-L 140. μm	N160 160. μm
0.5.........	0.47	3.73E−28	1.77E−28	4.38E−27	3.54E−27	3.45E−27	4.92E−27	5.39E−27	5.93E−27	4.46E−26	8.43E−26	1.32E−25	1.26E−25
	1.12	1.02E−27	4.94E−28	1.03E−26	7.55E−27	6.29E−27	6.57E−27	6.32E−27	6.22E−27	4.20E−26	8.02E−26	1.28E−25	1.22E−25
	1.77	1.68E−27	8.14E−28	1.62E−26	1.16E−26	9.17E−27	8.23E−27	7.25E−27	6.49E−27	3.99E−26	7.73E−26	1.25E−25	1.20E−25
	3.19	3.14E−27	1.54E−27	2.95E−26	2.10E−26	1.61E−26	1.29E−26	1.06E−26	8.56E−27	3.62E−26	7.04E−26	1.18E−25	1.13E−25
	4.58	4.64E−27	2.27E−27	4.33E−26	3.06E−26	2.34E−26	1.80E−26	1.43E−26	1.10E−26	3.25E−26	6.31E−26	1.10E−25	1.06E−25
1.0.........	0.47	7.45E−28	3.55E−28	8.76E−27	7.09E−27	6.92E−27	9.95E−27	1.10E−26	1.22E−26	1.23E−25	2.03E−25	2.48E−25	2.25E−25
	1.12	2.04E−27	9.87E−28	2.06E−26	1.51E−26	1.26E−26	1.32E−26	1.28E−26	1.28E−26	1.16E−25	1.93E−25	2.40E−25	2.19E−25
	1.77	3.35E−27	1.63E−27	3.25E−26	2.32E−26	1.84E−26	1.66E−26	1.47E−26	1.33E−26	1.11E−25	1.87E−25	2.36E−25	2.16E−25
	3.19	6.27E−27	3.07E−27	5.90E−26	4.19E−26	3.23E−26	2.59E−26	2.13E−26	1.74E−26	1.01E−25	1.71E−25	2.22E−25	2.04E−25
	4.58	9.28E−27	4.54E−27	8.66E−26	6.13E−26	4.68E−26	3.62E−26	2.87E−26	2.22E−26	8.97E−26	1.55E−25	2.09E−25	1.93E−25
3.0.........	0.47	2.23E−27	1.06E−27	2.63E−26	2.14E−26	2.09E−26	3.10E−26	3.49E−26	3.97E−26	5.66E−25	7.27E−25	5.93E−25	5.01E−25
	1.12	6.11E−27	2.96E−27	6.18E−26	4.54E−26	3.80E−26	4.08E−26	4.03E−26	4.12E−26	5.38E−25	6.98E−25	5.78E−25	4.89E−25
	1.77	1.01E−26	4.88E−27	9.76E−26	6.98E−26	5.52E−26	5.06E−26	4.57E−26	4.25E−26	5.19E−25	6.80E−25	5.71E−25	4.84E−25
	3.19	1.88E−26	9.21E−27	1.77E−25	1.26E−25	9.71E−26	7.87E−26	6.56E−26	5.48E−26	4.73E−25	6.28E−25	5.43E−25	4.61E−25
	4.58	2.78E−26	1.36E−26	2.60E−25	1.84E−25	1.40E−25	1.09E−25	8.79E−26	6.95E−26	4.24E−25	5.76E−25	5.17E−25	4.42E−25
5.0.........	0.47	3.72E−27	1.77E−27	4.40E−26	3.57E−26	3.52E−26	5.31E−26	6.08E−26	7.02E−26	1.09E−24	1.25E−24	8.52E−25	6.96E−25
	1.12	1.02E−26	4.93E−27	1.03E−25	7.58E−26	6.36E−26	6.94E−26	6.97E−26	7.23E−26	1.04E−24	1.20E−24	8.32E−25	6.80E−25
	1.77	1.68E−26	8.13E−27	1.63E−25	1.16E−25	9.23E−26	8.57E−26	7.85E−26	7.43E−26	1.00E−24	1.17E−24	8.23E−25	6.74E−25
	3.19	3.14E−26	1.54E−26	2.95E−25	2.10E−25	1.62E−25	1.32E−25	1.12E−25	9.47E−26	9.18E−25	1.09E−24	7.85E−25	6.45E−25
	4.58	4.64E−26	2.27E−26	4.33E−25	3.07E−25	2.34E−25	1.84E−25	1.49E−25	1.19E−25	8.29E−25	1.01E−24	7.53E−25	6.22E−25
10.0.......	0.47	7.45E−27	3.55E−27	8.82E−26	7.19E−26	7.16E−26	1.12E−25	1.31E−25	1.54E−25	2.48E−24	2.50E−24	1.36E−24	1.06E−24
	1.12	2.04E−26	9.87E−27	2.06E−25	1.52E−25	1.28E−25	1.44E−25	1.48E−25	1.58E−25	2.37E−24	2.41E−24	1.33E−24	1.04E−24
	1.77	3.35E−26	1.63E−26	3.26E−25	2.33E−25	1.85E−25	1.76E−25	1.65E−25	1.61E−25	2.30E−24	2.36E−24	1.32E−24	1.04E−24
	3.19	6.27E−26	3.07E−26	5.90E−25	4.20E−25	3.25E−25	2.70E−25	2.31E−25	2.01E−25	2.12E−24	2.21E−24	1.26E−24	9.96E−25
	4.58	9.28E−26	4.54E−26	8.67E−25	6.14E−25	4.70E−25	3.73E−25	3.06E−25	2.50E−25	1.93E−24	2.06E−24	1.22E−24	9.65E−25
100.0.....	0.47	7.46E−26	3.56E−26	9.28E−25	7.90E−25	8.63E−25	1.62E−24	2.08E−24	2.76E−24	2.55E−23	1.77E−23	4.84E−24	3.36E−24
	1.12	2.04E−25	9.90E−26	2.11E−24	1.59E−24	1.42E−24	1.91E−24	2.20E−24	2.72E−24	2.47E−23	1.72E−23	4.75E−24	3.30E−24
	1.77	3.36E−25	1.63E−25	3.30E−24	2.40E−24	1.98E−24	2.19E−24	2.32E−24	2.68E−24	2.43E−23	1.70E−23	4.73E−24	3.29E−24
	3.19	6.28E−25	3.08E−25	5.96E−24	4.27E−24	3.37E−24	3.11E−24	2.94E−24	3.00E−24	2.29E−23	1.62E−23	4.60E−24	3.20E−24
	4.58	9.29E−25	4.55E−25	8.74E−24	6.22E−24	4.84E−24	4.17E−24	3.69E−24	3.43E−24	2.15E−23	1.55E−23	4.51E−24	3.15E−24

[a] Additional models, with spectra, are available online at http://www.astro.princeton.edu/~draine/dust/irem.html.

The following weighted sum of IRAC 7.9 μm and the three MIPS bands is a reasonably accurate estimator for $L_{\rm TIR}$:

$$L_{\rm TIR} \approx 0.95\langle \nu L_\nu \rangle_{7.9} + 1.15\langle \nu L_\nu \rangle_{24} + \langle \nu L_\nu \rangle_{71} + \langle \nu L_\nu \rangle_{160}. \quad (22)$$

Figure 17 plots this estimator relative to the actual $L_{\rm TIR}$ for our dust models, showing that equation (22) allows the total infrared luminosity to be estimated to within $\sim$10% for our dust models heated by starlight with $0.1 \lesssim U \lesssim 10^2$ or with $10^4 \lesssim U \lesssim 10^6$. The accuracy becomes somewhat lower for $10^2 \lesssim U \lesssim 10^4$ (because of the factor of 3 gap in wavelength between the 71 μm band and the 24 μm band), but the worst-case error is only $\sim$30%, occurring for $U \approx 10^3$ where the FIR emission peak falls at $\sim$40 μm, halfway between the MIPS 24 and 71 μm filters, with the result that MIPS photometry underestimates the actual power. Also plotted in Figure 17 is the TIR estimator proposed by Dale & Helou (2002) using only MIPS photometry, applied to our models. The Dale & Helou (2002) luminosity estimate is accurate to within $\pm$25% for $U \lesssim 10^2$.

8. EMISSION SPECTRA FOR DUST MODELS: DISTRIBUTION OF STARLIGHT INTENSITIES

The dust grains in a galaxy will be exposed to a wide range of starlight intensities. The bulk of the dust in the diffuse ISM will be heated by a general diffuse radiation field contributed by many stars. However, some dust grains will happen to be located in regions close to luminous stars, such as PDRs near OB stars, where the starlight heating the dust will be much more intense than the diffuse starlight illuminating the bulk of the grains.

In principle, one could construct a model for the distribution of stars and dust in the galaxy and solve the radiative transfer problem to determine the heating rate for each dust grain. This, however, requires many uncertain assumptions, as well as heavy numerical calculations to solve the radiative transfer problem (see, e.g., Witt & Gordon 1996; Silva et al. 1998; Popescu et al. 2000; Tuffs et al. 2004; Piovan et al. 2006). Here we take a much simpler approach and assume a simple parametric form for the fraction of the dust mass exposed to a distribution of starlight intensities U described by a delta function and a power-law distribution for $U_{\rm min} < U < U_{\rm max}$:

$$\frac{dM_{\rm dust}}{dU} = (1-\gamma)M_{\rm dust}\delta(U - U_{\rm min}) + \gamma M_{\rm dust}\frac{(\alpha - 1)}{\left(U_{\rm min}^{1-\alpha} - U_{\rm max}^{1-\alpha}\right)}U^{-\alpha}, \quad \alpha \neq 1, \quad (23)$$

where $dM_{\rm dust}$ is the mass of dust heated by starlight intensities in $[U, U + dU]$, $M_{\rm dust}$ is the total mass of dust, $(1-\gamma)$ is the fraction of the dust mass that is exposed to starlight intensity $U_{\rm min}$, and α is a power-law index. This functional form is similar to the power-law distribution used by Dale et al. (2001) and Dale & Helou (2002), except that we have added a delta-function component that contains most of the dust mass; the delta-function term is intended to represent the dust in the general diffuse ISM.

The starlight distribution function equation (23) has parameters $U_{\rm min}$, $U_{\rm max}$, α, and γ. However, Draine et al. (2007) find that

TABLE 6

Model Emissivities $\langle \nu j_\nu \rangle_{\rm band}$ (ergs s^{-1} sr^{-1} H^{-1})[a] for Herschel

U	$q_{\rm PAH}$ (%)	PACS 1 75 μm	PACS 2 110 μm	PACS 3 170 μm	SPIRE 1 250 μm	SPIRE 2 360 μm	SPIRE 3 520 μm
0.5	0.47	4.21E−26	7.92E−26	9.61E−26	5.71E−26	2.05E−26	5.80E−27
	1.12	3.97E−26	7.57E−26	9.31E−26	5.58E−26	2.01E−26	5.70E−27
	1.77	3.78E−26	7.34E−26	9.17E−26	5.53E−26	2.00E−26	5.68E−27
	3.19	3.43E−26	6.71E−26	8.61E−26	5.28E−26	1.92E−26	5.50E−27
	4.58	3.05E−26	6.05E−26	8.09E−26	5.07E−26	1.87E−26	5.39E−27
1.0	0.47	1.13E−25	1.78E−25	1.73E−25	8.74E−26	2.83E−26	7.50E−27
	1.12	1.08E−25	1.71E−25	1.68E−25	8.55E−26	2.77E−26	7.38E−27
	1.77	1.03E−25	1.67E−25	1.66E−25	8.48E−26	2.76E−26	7.35E−27
	3.19	9.33E−26	1.53E−25	1.57E−25	8.13E−26	2.66E−26	7.13E−27
	4.58	8.32E−26	1.40E−25	1.48E−25	7.85E−26	2.60E−26	7.01E−27
3.0	0.47	4.96E−25	5.69E−25	3.94E−25	1.56E−25	4.40E−26	1.07E−26
	1.12	4.73E−25	5.49E−25	3.84E−25	1.53E−25	4.32E−26	1.05E−26
	1.77	4.57E−25	5.37E−25	3.80E−25	1.52E−25	4.30E−26	1.05E−26
	3.19	4.17E−25	5.00E−25	3.62E−25	1.47E−25	4.17E−26	1.02E−26
	4.58	3.76E−25	4.64E−25	3.47E−25	1.43E−25	4.09E−26	1.01E−26
5.0	0.47	9.28E−25	9.23E−25	5.54E−25	1.99E−25	5.29E−26	1.25E−26
	1.12	8.87E−25	8.92E−25	5.41E−25	1.95E−25	5.20E−26	1.23E−26
	1.77	8.59E−25	8.75E−25	5.36E−25	1.94E−25	5.18E−26	1.22E−26
	3.19	7.89E−25	8.20E−25	5.12E−25	1.88E−25	5.03E−26	1.19E−26
	4.58	7.17E−25	7.67E−25	4.93E−25	1.83E−25	4.94E−26	1.18E−26
10.0	0.47	2.04E−24	1.71E−24	8.59E−25	2.73E−25	6.77E−26	1.53E−26
	1.12	1.96E−24	1.66E−24	8.41E−25	2.68E−25	6.67E−26	1.51E−26
	1.77	1.91E−24	1.63E−24	8.35E−25	2.67E−25	6.64E−26	1.50E−26
	3.19	1.76E−24	1.54E−24	8.02E−25	2.59E−25	6.47E−26	1.47E−26
	4.58	1.62E−24	1.45E−24	7.77E−25	2.54E−25	6.36E−26	1.45E−26
100.0	0.47	1.88E−23	9.29E−24	2.84E−24	6.49E−25	1.35E−25	2.75E−26
	1.12	1.82E−23	9.08E−24	2.79E−24	6.40E−25	1.33E−25	2.71E−26
	1.77	1.79E−23	9.00E−24	2.78E−24	6.38E−25	1.33E−25	2.71E−26
	3.19	1.70E−23	8.66E−24	2.71E−24	6.24E−25	1.30E−25	2.66E−26
	4.58	1.61E−23	8.39E−24	2.66E−24	6.17E−25	1.29E−25	2.64E−26

[a] Additional models, with spectra, are available online at http://www.astro.princeton.edu/~draine/dust/irem.html.

the spectral energy distributions of galaxies in SINGS appear to be satisfactorily reproduced with fixed $\alpha = 2$ and $U_{\rm max} = 10^6$, and we therefore use these fixed values for α and $U_{\rm max}$. For $\alpha = 2$ the fraction γ of the dust mass that is exposed to starlight intensities $U_{\rm min} < U \le U_{\rm max}$ has equal amounts of infrared power per unit log U. Each of the grain models in Table 3 has a different value of $q_{\rm PAH}$, so the parameter $q_{\rm PAH}$ serves as a proxy for the dust model. This leaves us with four free parameters: $M_{\rm dust}$, $q_{\rm PAH}$, $U_{\rm min}$, and γ. The shape of the dust emission spectrum is determined by only three free parameters: $q_{\rm PAH}$, $U_{\rm min}$, and γ. Examples of emission spectra are shown in Figure 18.

9. ESTIMATING $q_{\rm PAH}$, $U_{\rm min}$, γ, $f_{\rm PDR}$, AND $M_{\rm dust}$

Photometry obtained with the IRAC and MIPS cameras on *Spitzer* can be used to estimate the free parameters $q_{\rm PAH}$, $U_{\rm min}$, and γ, the fraction $f_{\rm PDR}$ of the dust infrared emission radiated by dust grains in PDRs where $U > 10^2$, and the total dust mass $M_{\rm dust}$. The flux measured in the IRAC 3.6 μm band is almost entirely due to starlight and therefore can be used to remove the starlight contribution to the 7.9 and 24 μm bands, with the nonstellar flux densities estimated to be

$$F_\nu^{\rm ns}(7.9\ \mu{\rm m}) = F_\nu(7.9\ \mu{\rm m}) - 0.232 F_\nu(3.6\ \mu{\rm m}), \quad (24)$$

$$F_\nu^{\rm ns}(24\ \mu{\rm m}) = F_\nu(24\ \mu{\rm m}) - 0.032 F_\nu(3.6\ \mu{\rm m}), \quad (25)$$

where the coefficients 0.232 and 0.032 are from Helou et al. (2004). The stellar contribution to the 71 and 160 μm bands is negligible.

For a given dust type (i.e., a given value of $q_{\rm PAH}$) there is a two-dimensional family of emission models, parameterized by $U_{\rm min}$ and γ. Figures 19*a* and 19*b* show the flux into the MIPS 24 μm band normalized by the total dust luminosity $L_{\rm TIR}$, plotted against the ratio of the fluxes into the MIPS 71 and 160 μm bands. The two-dimensional family of emission models is shown, for $0.1 \le U_{\rm min} \le 20$ and $0 \le \gamma \le 0.20$. The models with $\gamma = 0$ (the lower boundary of the model grid) are models with dust heated by a single starlight intensity: $\langle U \rangle = U_{\rm min}$.

For the $\gamma = 0$ models, the ratio $\langle \nu L_\nu \rangle_{24}/L_{\rm TIR}$ is essentially independent of $U_{\rm min}$ for $U_{\rm min} \lesssim 2$, as already seen in Figure 15: the emission into the 24 μm band is dominated by single-photon heating of small grains. For $\gamma > 0$, some fraction of the dust is exposed to starlight intensities $U \gtrsim 10$, and the fraction of the total power that enters the 24 μm band increases. For the particular size distributions that have been adopted for these models (see Fig. 11), the models with $q_{\rm PAH} = 0.47\%$ and 4.6% (Figs. 19*a* and 19*b*) differ by only a factor of $\sim$1.5 in $\langle \nu L_\nu \rangle_{24}/L_{\rm TIR}$ in the single-photon heating limit ($U_{\rm min} < 1$, $\gamma = 0$).

The emission into the 7.9 μm band is a different story. Figures 19*c* and 19*d* show that in the single-photon heating limit, the fraction of the power radiated into the 7.9 μm band is essentially proportional to $q_{\rm PAH}$: as $q_{\rm PAH}$ increases from 0.47% to 4.6%, $\langle \nu L_\nu \rangle_{7.9}/L_{\rm TIR}$ increases from 0.02 to 0.2. As γ is increased, some additional 7.9 μm emission is produced; this results in a noticeable fractional increase for the $q_{\rm PAH} = 0.47\%$ model, but for the $q_{\rm PAH} = 4.6\%$ model the additional emission produces a very small fractional change in $\langle \nu L_\nu \rangle_{7.9}/L_{\rm TIR}$, which remains dominated by single-photon heating.

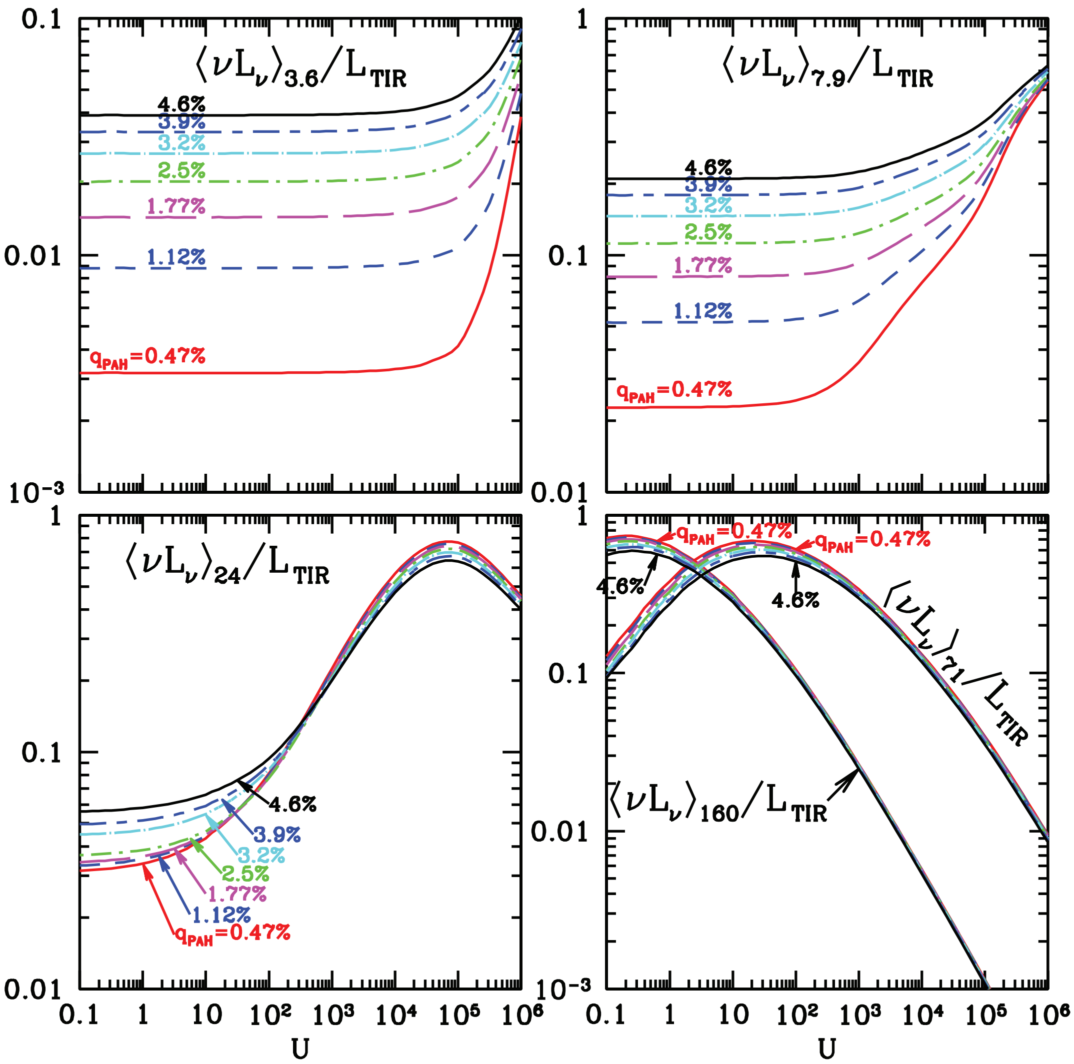

FIG. 15.—IRAC 3.6 μm, IRAC 7.9 μm, MIPS 24 μm, MIPS 71 μm, and MIPS 160 μm band strengths for dust illuminated by a single starlight intensity U, as a function of U, for dust models with seven different values of $q_{\rm PAH}$.

To determine $q_{\rm PAH}$, $U_{\rm min}$, γ, and $M_{\rm dust}$, the best procedure is to vary all the parameters to find the dust model that comes closest to reproducing the photometry. This procedure is used by Draine et al. (2007) in their study of the dust properties of the SINGS galaxy sample.

However, it is also possible to use a graphical procedure to find values of $q_{\rm PAH}$, $U_{\rm min}$, and γ that are consistent with the observed data. We assume that we have *Spitzer* photometry in five bands: the 3.6 and 7.9 μm bands of IRAC and the 24, 71, and 160 μm bands of MIPS. The 3.6 μm band observations are used with equations (24) and (25) to obtain $\langle F_\nu^{\rm ns}\rangle_{7.9}$ and $\langle F_\nu^{\rm ns}\rangle_{24}$. We define three ratios of observables:

$$P_{7.9} \equiv \frac{\langle \nu F_\nu^{\rm ns}\rangle_{7.9}}{\langle \nu F_\nu\rangle_{71} + \langle \nu F_\nu\rangle_{160}}, \qquad (26)$$

$$P_{24} \equiv \frac{\langle \nu F_\nu^{\rm ns}\rangle_{24}}{\langle \nu F_\nu\rangle_{71} + \langle \nu F_\nu\rangle_{160}}, \qquad (27)$$

$$R_{71} \equiv \frac{\langle \nu F_\nu\rangle_{71}}{\langle \nu F_\nu\rangle_{160}}. \qquad (28)$$

For starlight intensities $0.1 \lesssim U \lesssim 10^2$, the bulk of the power radiated by dust emerges in the 50–200 μm wavelength range, and therefore the total dust luminosity is approximately proportional to $[\langle \nu F_\nu\rangle_{71} + \langle \nu F_\nu\rangle_{160}]$. The ratio R_{71} is sensitive to the temperature of the $a \gtrsim 0.01$ μm grains that dominate the FIR emission; R_{71} is therefore an indicator for the intensity of the starlight heating the dust.

9.1. *Determining the PAH Fraction* $q_{\rm PAH}$

$P_{7.9}$ is proportional to the fraction of the dust power radiated in the PAH features. Because the 7.9 μm emission is almost entirely the result of single-photon heating, $P_{7.9}$ depends very weakly on the starlight intensity.

Figure 20 shows $P_{7.9}$ versus R_{71} for a sequence of grain models, each with a different PAH abundance $q_{\rm PAH}$. The model with the lowest value of $q_{\rm PAH}$ naturally has very low values of $P_{7.9}$. Because of the very low PAH abundance in Figure 20*a*, a very small amount of dust exposed to high values of U can enhance the 8 μm emission, and therefore $P_{7.9}$ increases notably as γ increases from 0, with increasing amounts of dust exposed to radiation intensities between $U_{\rm min}$ and $U_{\rm max} = 10^6$. However, as $q_{\rm PAH}$ is increased, $P_{7.9}$ becomes less sensitive to γ because single-photon

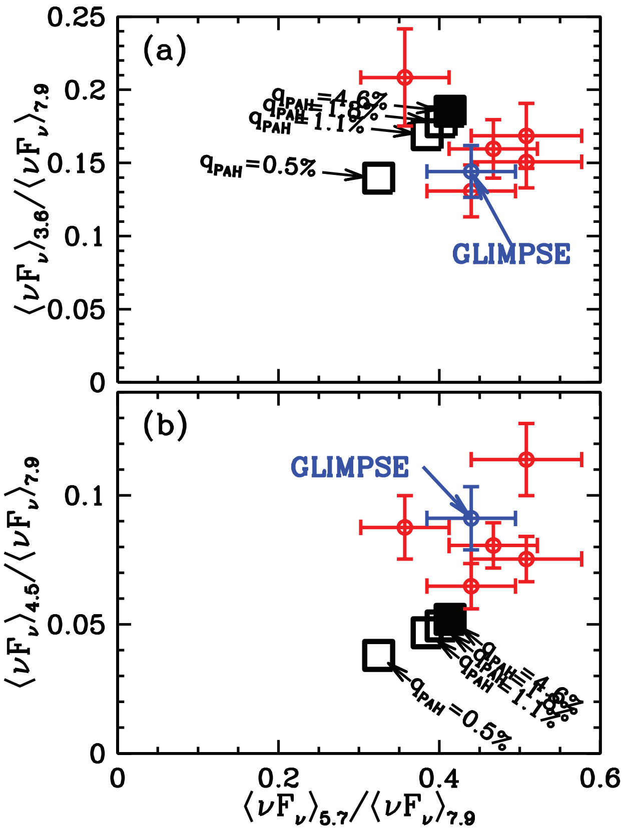

FIG. 16.—IRAC color-color plots for dust emission. *Symbols with error bars*: Diffuse emission extracted by Flagey et al. (2006) for five GFLS fields and for one GLIMPSE field. *Squares*: Present models for Milky Way dust with different values of $q_{\rm PAH} = 0.47\%$, 1.1%, 1.8%, and 4.6%, for starlight intensities $U \lesssim 10^3$ so that single-photon heating is dominant. The dust model appears consistent with the observed diffuse emission in IRAC 3.6, 5.7, and 7.9 μm bands, but observed emission in the 4.5 μm band appears to be about 50% stronger than given by the model emissivities.

heating of the PAHs produces 7.9 μm emission even when U is small.

Based on modeling many spectra, we expect that the 7.9 μm emission will primarily arise from single-photon heating, i.e., $P_{7.9}$ will be close to the value calculated for $\gamma = 0$. The approximate value of $q_{\rm PAH}$ can therefore be determined by finding a dust model among Figures 20*a*–20*g* for which the observed $(R_{71},\ P_{7.9})$ point falls just above the $\gamma = 0$ curve. The location $(R_{71},\ P_{7.9})$ on the appropriate plot also gives an estimate for $U_{\rm min}$ and γ, but these parameters are better determined using the 24 μm emission, as described below.

9.2. *Determining* $U_{\rm min}$ *and* γ

P_{24} is proportional to the fraction of the dust power radiated near 24 μm. As seen in Figure 7, 24 μm emission can be produced by single-photon heating of $a \approx 15$–40 Å grains. For a given dust model there is therefore a limiting value of P_{24} that applies for $0.1 \lesssim U \lesssim 10$ where the bulk of the dust power is captured in the 71 and 160 μm bands. However, when some fraction of the grains are heated by starlight with intensities $U \gtrsim 20$ (see Fig. 15), larger dust grains can be heated sufficiently to add to the 24 μm emission. As a result, R_{24} is sensitive to the value of γ.

To estimate the value of γ, one looks for a dust model in Figure 21 with the value of $q_{\rm PAH}$ found from Figure 20. The observed location of $(R_{71},\ P_{24})$ on Figure 21 then allows $U_{\rm min}$ and γ to be determined. It may happen that $(U_{\rm min},\ \gamma)$ estimated from Figure 21 differs from $(U_{\rm min},\ \gamma)$ indicated by Figure 20. When this occurs, it is an indication that a single dust model does not perfectly reproduce the observed 7.9, 24, 71, and 160 μm colors. We recommend using the values of $(U_{\rm min},\ \gamma)$ estimated from Figure 21 as they are less sensitive to the adopted value of $q_{\rm PAH}$.

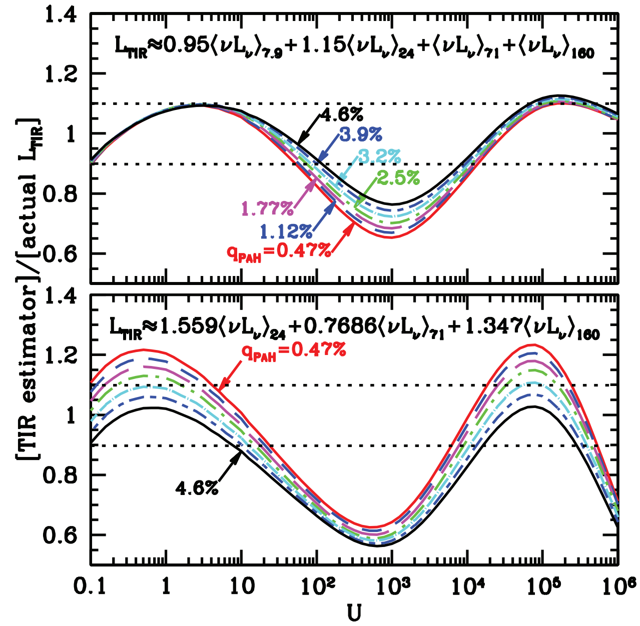

FIG. 17.—*Top*: Estimator (eq. [22]) for TIR divided by actual TIR. The estimator given by eq. (22) is within ±10% of the actual TIR (within the dotted lines) for $0.1 < U \lesssim 10^2$ and $10^4 \lesssim U < 10^6$. *Bottom*: TIR estimator from Dale & Helou (2002), applied to the present dust models.

9.3. *Determining* $f_{\rm PDR}$

Young stars tend to be in or near to dust clouds. In star-forming galaxies such as the Milky Way, we expect that a significant fraction of the starlight emitted by O and B stars will be absorbed by dust that happens to be relatively close to the star, so that the starlight intensity is significantly above the average starlight intensity. PDRs are typical examples of such environments.

For the power-law distribution of starlight intensities given by equation (23) with $\alpha = 2$, we can calculate a quantity $f_{\rm PDR}$, which we define here as the fraction of the total dust luminosity that is radiated by dust grains in regions where $U > 10^2$:

$$f_{\rm PDR} = \frac{\gamma \ln(U_{\rm max}/10^2)}{(1-\gamma)(1-U_{\rm min}/U_{\rm max}) + \gamma \ln(U_{\rm max}/U_{\rm min})}. \quad (29)$$

If $U_{\rm min}$ and γ are known [e.g., determined either by finding the best-fit $(q_{\rm PAH},\ U_{\rm min},\ \gamma)$ from the three-dimensional model space or by following the graphical procedures described above], $f_{\rm PDR}$ can be calculated from equation (29). Here we show how $f_{\rm PDR}$ can be estimated directly from IRAC and MIPS photometry.

For the Milky Way dust models considered here, PAHs undergoing single-photon heating convert a small fraction of the absorbed starlight power into 24 μm emission, but when a distribution of starlight intensities is present, there is additional

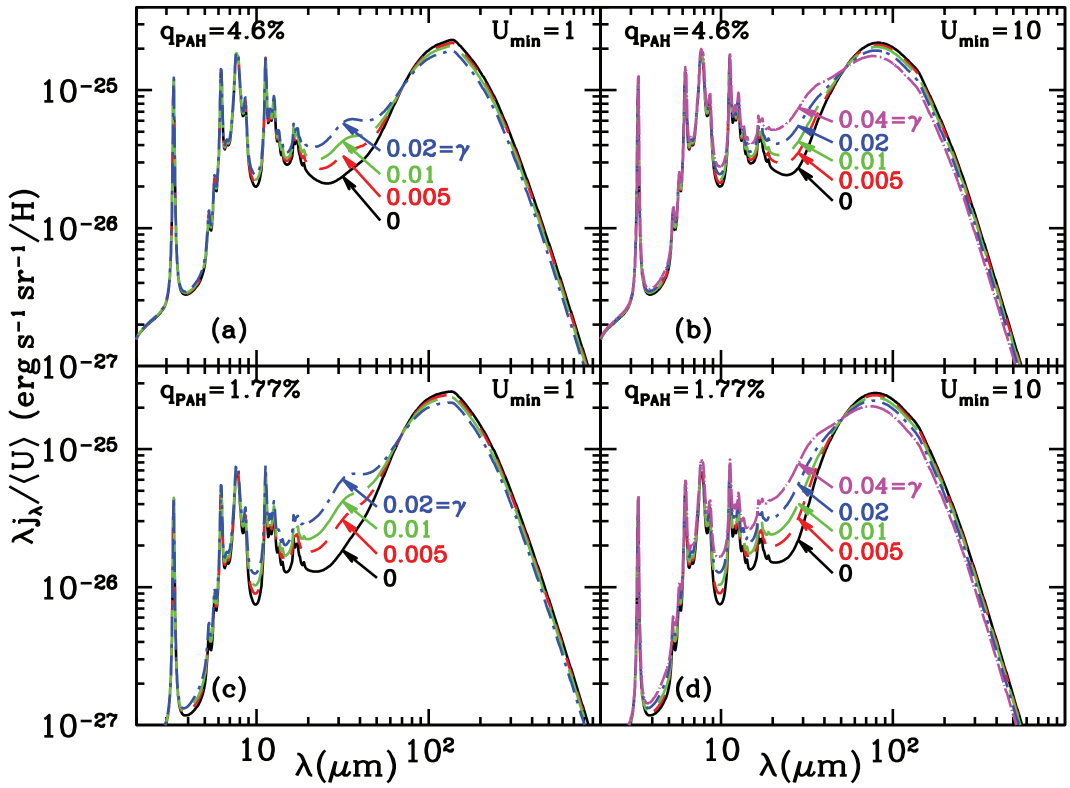

FIG. 18.—Emission spectra for models with MW dust with (*a*) $q_{\rm PAH} = 4.6\%$, $U_{\rm min} = 1$, (*b*) $q_{\rm PAH} = 4.6\%$, $U_{\rm min} = 10$, (*c*) $q_{\rm PAH} = 1.77\%$, $U_{\rm min} = 1$, (*d*) $q_{\rm PAH} = 1.77\%$, $U_{\rm min} = 10$. All models have $U_{\rm max} = 10^6$, $\alpha = 2$. Values of γ are indicated.

24 μm emission from high-intensity regions. The 24 μm contribution from PAHs depends, of course, on the PAH abundance. We find that for our models $f_{\rm PDR}$ can be closely related to the fraction of the power radiated at 24 μm after subtraction of the contribution of PAHs to the 24 μm power. We find that the combination $(P_{24} - 0.14P_{7.9})$ gives a quantity that is sensitive to U and relatively insensitive to the value of $q_{\rm PAH}$.

Figure 22 shows $f_{\rm PDR}$ versus $P_{24} - 0.14P_{7.9}$ for eight different dust models with different values of $q_{\rm PAH}$ and $U_{\rm min}$. We see that the curves fall within a narrow band. For these dust models, $f_{\rm PDR}$ can be estimated from the observable $P_{24} - 0.14P_{7.9}$ using Figure 22.

9.4. *Examples*

To illustrate this, five galaxies are indicated in Figures 20 and 21: NGC 1266, NGC 3521, NGC 6822, IC 2574, and Mrk 33. Table 7 gives the measured global fluxes for these galaxies (Dale et al. 2005); the derived ratios $P_{7.9}$, P_{24}, and R_{71}; and the values of $q_{\rm PAH}$, $U_{\rm min}$, and γ obtained from the procedure described in §§ 9.1 and 9.2. Below we comment on the individual cases.

IC 2574.—In Figure 20, the very low value of $P_{7.9} = 0.027$ only falls on the model grid in Figure 20*a*; therefore, we select $q_{\rm PAH} = 0.5\%$. From Figure 21*a*, we find $U_{\rm min} \approx 2.3$ and $\gamma \approx 0.012$.

Mrk 33.—From Figure 20*e* we estimate $q_{\rm PAH} \approx 3.2\%$. The very high value of $P_{24} = 0.46$ requires $U_{\rm min} \approx 7$ and $\gamma \approx 0.14$ on Figure 21*e* in order to have enough hot dust to reproduce the observed 24 μm flux. The very large value found for γ suggests that a large fraction of the dust heating in Mrk 33 is taking place in PDRs near OB associations, consistent with the dwarf starburst nature of this galaxy (Hunt et al. 2005).

NGC 1266.—The low value of $P_{7.9} \approx 0.044$ can only be reproduced in Figure 20 by models with small values of $q_{\rm PAH}$. Of the values of $q_{\rm PAH}$ for which spectra have been computed, $q_{\rm PAH} = 0.47\%$ is preferred. Turning now to Figure 21*a*, we find that $U_{\rm min} \approx 12.5$ and $\gamma \approx 0.029$. The values of $q_{\rm PAH}$, $U_{\rm min}$, and γ found by this graphical exercise are in good agreement with the best-fit values of $q_{\rm PAH} = 0.47\%$, $U_{\rm min} = 12$, and $\gamma = 0.029$ (Draine et al. 2007).

NGC 3521.—From Figure 20*g* we find $q_{\rm PAH} \approx 4.6\%$. From Figure 21*g* we obtain $U_{\rm min} \approx 1.1$ and $\gamma \approx 0.007$. SCUBA fluxes are also available for this galaxy (Dale et al. 2005); when the 850 μm flux is used to constrain the grain model, Draine et al. (2007) find that it is difficult to simultaneously reproduce the MIPS and SCUBA photometry. The overall best fit is found for $U_{\rm min} = 2$, $\gamma = 0.01$.

NGC 6822.—From Figure 20*b* we estimate $q_{\rm PAH} = 1.1\%$. From Figure 21*g* we estimate $U_{\rm min} \approx 2.0$ and $\gamma \approx 0.006$. These are in agreement with the best-fit values $q_{\rm PAH} = 1.2\%$, $U_{\rm min} = 2.0$, and $\gamma = 0.005$ found by Draine et al. (2007).

9.5. *Estimating the Dust Mass $M_{\rm dust}$*

Consider a galaxy at distance D. If j_ν is the dust emissivity per H nucleon, then the flux is

$$F_\nu = \frac{M_{\rm H}}{m_{\rm H}} \frac{j_\nu}{D^2} \tag{30}$$

and the dust mass is

$$M_{\rm dust} = \left(\frac{M_{\rm dust}}{M_{\rm H}}\right) m_{\rm H} \frac{F_\nu}{j_\nu} D^2. \tag{31}$$

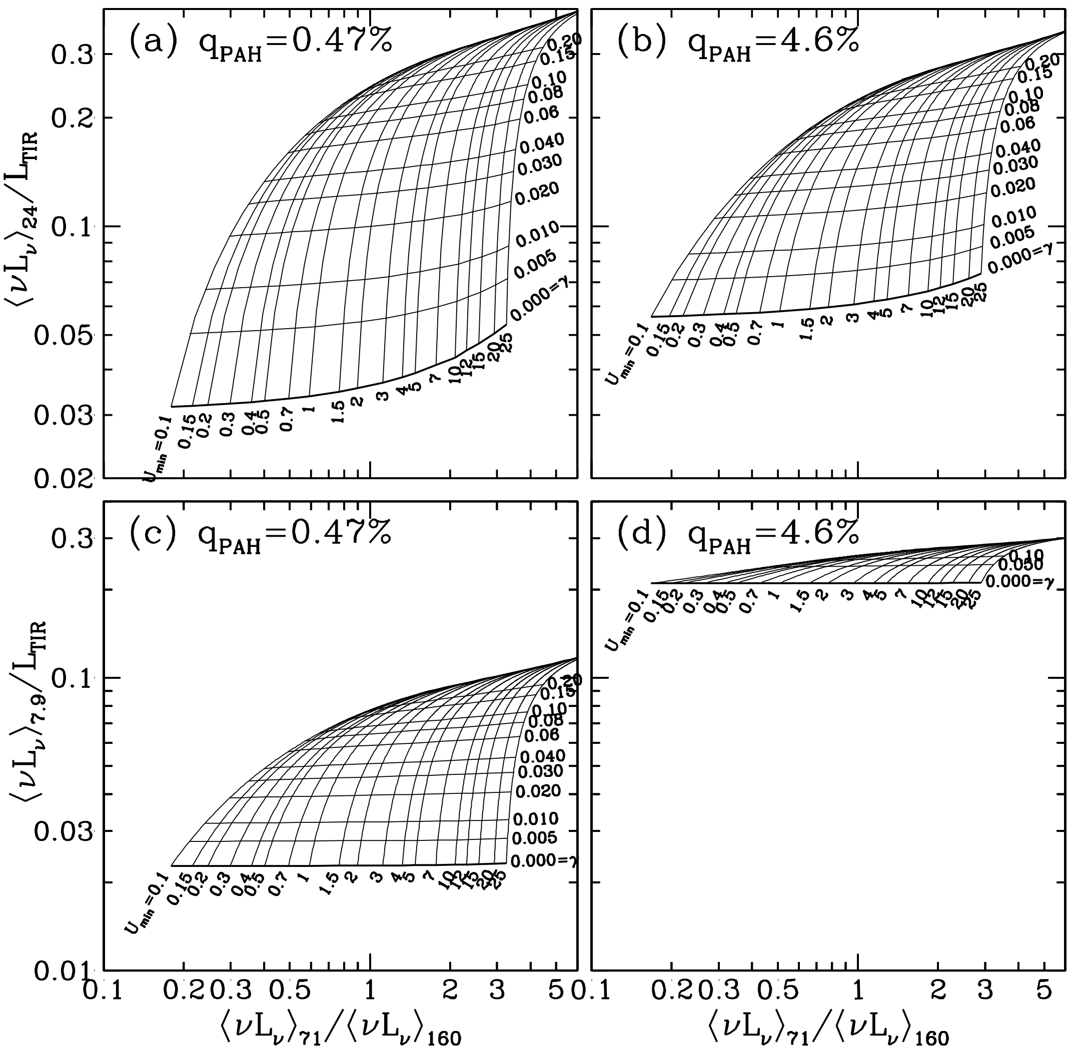

FIG. 19.—Ratios of $(\nu L_\nu)_{7.9}/L_{\rm TIR}$ and $(\nu L_\nu)_{24}/L_{\rm TIR}$ for dust models with $q_{\rm PAH} = 0.47\%$ and 4.6%, plotted against the ratio $(\nu L_\nu)_{71}/(\nu L_\nu)_{160}$. The model grids are labeled by the minimum starlight intensity $U_{\rm min}$ and the fraction γ of the dust exposed to starlight with $U > U_{\rm min}$ (see text).

If we know the values of $(M_{\rm dust}/M_{\rm H})$ and j_ν for a given grain model, we can estimate $M_{\rm dust}$ directly from the distance D and the observed flux F_ν. However, our estimate for j_ν may depend sensitively on our estimates for $q_{\rm PAH}$, $U_{\rm min}$, and γ.

A relatively robust approach to dust mass estimation is to note that for a given dust mixture the total dust luminosity is proportional to $M_{\rm dust}\langle U\rangle$. Define the quantity

$$\Psi(q_{\rm PAH},\,\gamma,\,U_{\rm min}) \equiv \left(\frac{M_{\rm dust}}{M_{\rm H}}\right) m_{\rm H}\frac{\langle U\rangle}{\langle \nu j_\nu\rangle_{24}+\langle \nu j_\nu\rangle_{71}+\langle \nu j_\nu\rangle_{160}}, \tag{32}$$

where $m_{\rm H}$ is the mass of an H atom and $\langle U\rangle$ is the mean starlight intensity. For the distribution function given by equation (23), with $\alpha = 2$, $\langle U\rangle$ is

$$\langle U\rangle \equiv \frac{\int U\,dM_{\rm dust}}{\int dM_{\rm dust}} = (1-\gamma)U_{\rm min} + \frac{\gamma U_{\rm min}\ln(U_{\rm max}/U_{\rm min})}{1-U_{\rm min}/U_{\rm max}}. \tag{33}$$

The dust mass is related to the observed fluxes by

$$M_{\rm dust} = \frac{\Psi}{\langle U\rangle}\left(\langle \nu F_\nu\rangle_{24}+\langle \nu F_\nu\rangle_{71}+\langle \nu F_\nu\rangle_{160}\right)D^2. \tag{34}$$

For a given dust model, we can calculate Ψ, which is shown in Figures 23*a*–23*g*. We observe that the values of Ψ in Figures 23*a*–23*g* range only from 0.044 to $\sim$0.066 g (ergs s^{-1})$^{-1}$, with $\Psi \approx 0.055$ g (ergs s^{-1})$^{-1}$ as a representative value. However, if we already have estimates for $q_{\rm PAH}$, $U_{\rm min}$, and γ, it is straightforward to obtain an accurate value for $\Psi(q_{\rm PAH},\,U_{\rm min},\,\gamma)$ from Figure 23.

To summarize, the procedure for estimating the dust mass $M_{\rm dust}$ is as follows:

1. Use $\langle F_\nu^{\rm ns}\rangle_{7.9}$, $\langle F_\nu^{\rm ns}\rangle_{24}$, $\langle F_\nu\rangle_{71}$, and $\langle F_\nu\rangle_{160}$ to calculate $P_{7.9}$, P_{24}, and R_{71}.
2. Use R_{71} and $P_{7.9}$ to estimate $q_{\rm PAH}$ by finding the value of $q_{\rm PAH}$ such that $(R_{71},\,P_{7.9})$ falls just above the $\gamma = 0$ curve in Figure 20.
3. Using this value of $q_{\rm PAH}$, locate $(R_{71},\,P_{24})$ on Figure 21 to determine $U_{\rm min}$ and γ.
4. Using the values of $q_{\rm PAH}$, $U_{\rm min}$, and γ, use Figure 23 to find Ψ.

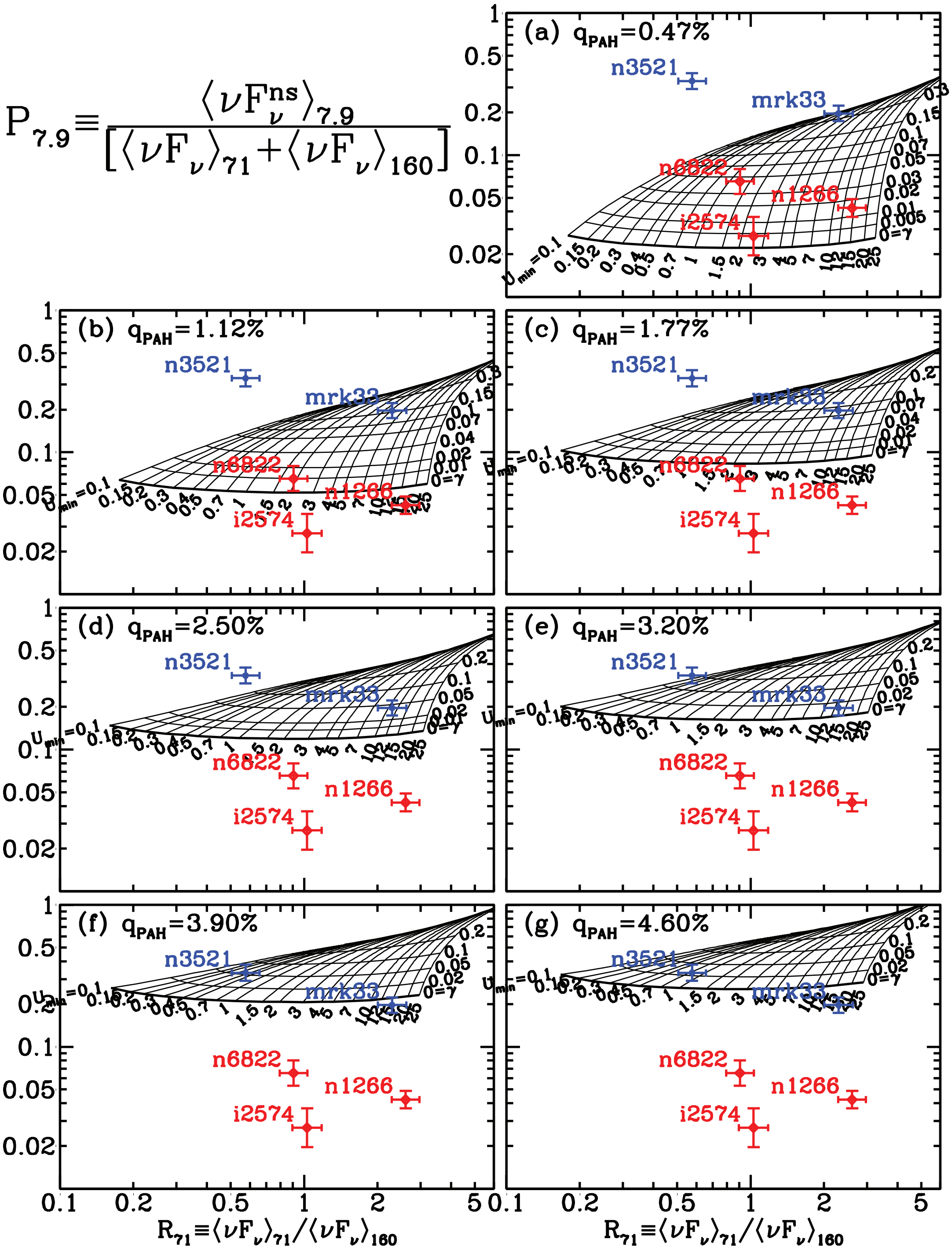

FIG. 20.—IRAC 7.9 μm power relative to MIPS 71 and 160 μm power vs. MIPS 71 μm/MIPS 160 μm band ratio.

5. Use $U_{\rm min}$ and γ (and $U_{\rm max} = 10^6$) to calculate $\langle U \rangle$ from equation (33).

6. Calculate $M_{\rm dust}$ using equation (34).

We have estimated $\langle U \rangle$, Ψ, and the resulting dust mass $M_{\rm dust}$ for the five sample galaxies, with results given in Table 7.

10. DISCUSSION

10.1. *Origin of Near-IR Continuum Opacity of PAHs*

The present models assume that the small-particle end of the grain size distribution is dominated by PAH particles, as assumed by WD01 and Li & Draine (2001a), and the PAH particles are therefore assumed to have a continuum component to $C_{\rm abs}$ in order to be able to reproduce 2–6 μm emission seen by *ISO* (Lu et al. 2003) and emission in the IRAC 4.5 μm filter (Helou et al. 2004). Continuum emission also appears to be present at other wavelengths, e.g., between the 12.6 and 16.45 μm features. In the 2–6 μm wavelength range, even very small carbonaceous grains are arbitrarily taken to have $C_{\rm abs}$ equal to 1% of the continuum that would be produced by free electron absorption in graphite, added to the discrete absorption bands expected for PAHs. The nature of this continuum absorption is unclear. Perhaps some PAHs, e.g., tubular PAHs with appropriate chirality (Zhou et al. 2006), have zero bandgap as in graphite.

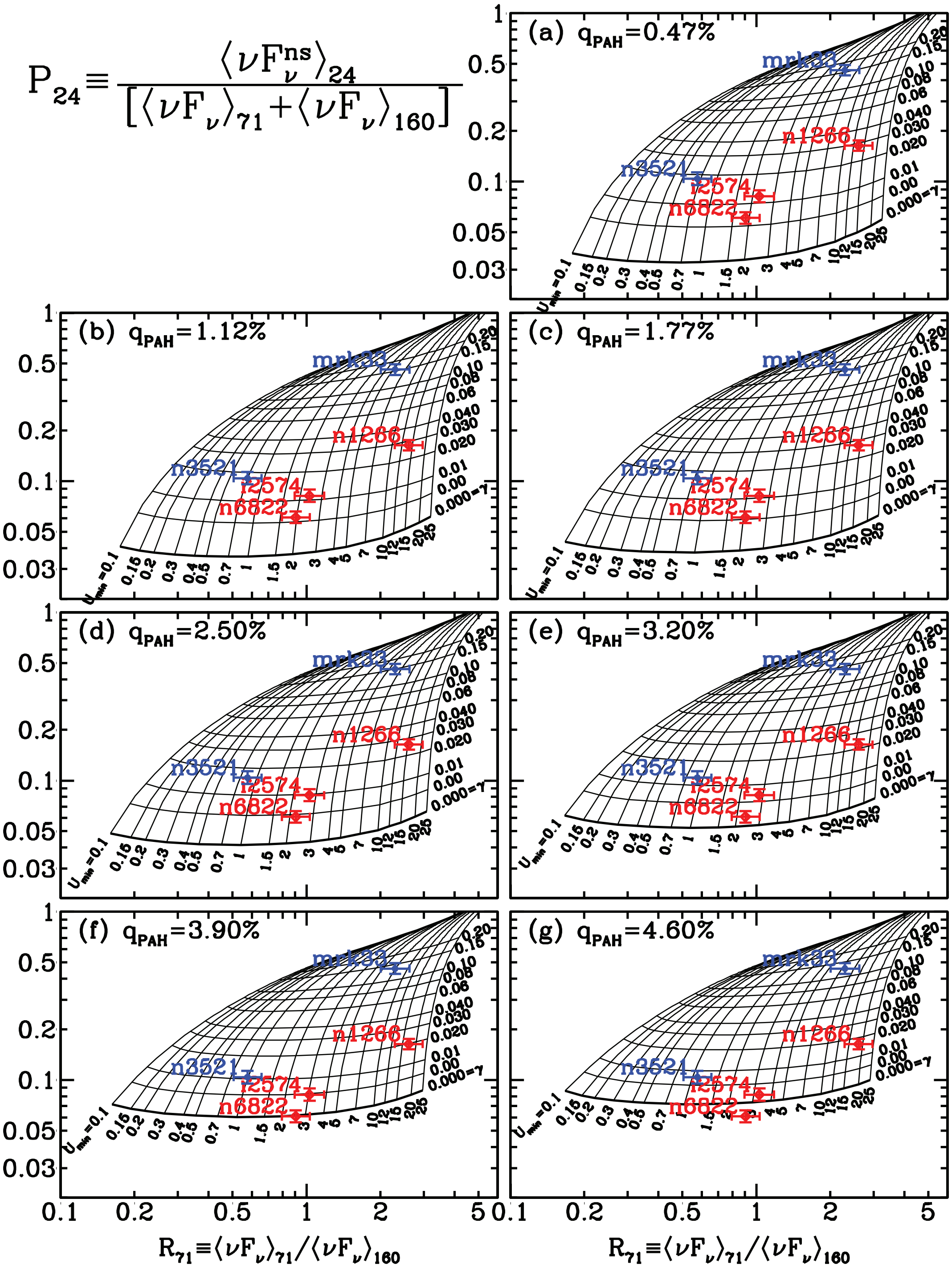

Fig. 21.—MIPS band ratios for models.

We are assuming that the PAHs are responsible for the 2–5 μm continuum. An & Sellgren (2003) find that the 2 μm continuum emission and 3.29 μm PAH emission have different spatial distributions in NGC 7023. Perhaps the 2 μm emission is strongest in regions where the PAHs have been dehydrogenated, thereby suppressing the 3.29 μm emission.

The assumption that the continuum emission originates in PAHs is consistent with the fact that the 9.8 and 18 μm silicate features are generally not seen in emission, except from regions (dusty winds, compact H II regions, dust near the Trapezium stars in Orion) where the starlight is thought to be sufficiently intense to heat $a \approx 0.1$ μm grains to $T \gtrsim 200$ K. However, Li & Draine (2001a) showed that the observed emission from the diffuse ISM in the Milky Way would in fact allow larger amounts of ultrasmall silicate grains than had been estimated previously because the 9.7 μm silicate emission feature can be "hidden" between the 8.6 and 11.3 μm PAH features.

In summary, the origin of the 2–5 μm continuum emission remains uncertain.

10.2. *Near-IR Absorption of PAH Ions: Astrophysical Implications*

The far-red to near-IR opacity of PAH ions described in LD01 was derived from earlier experimental data for a small number of

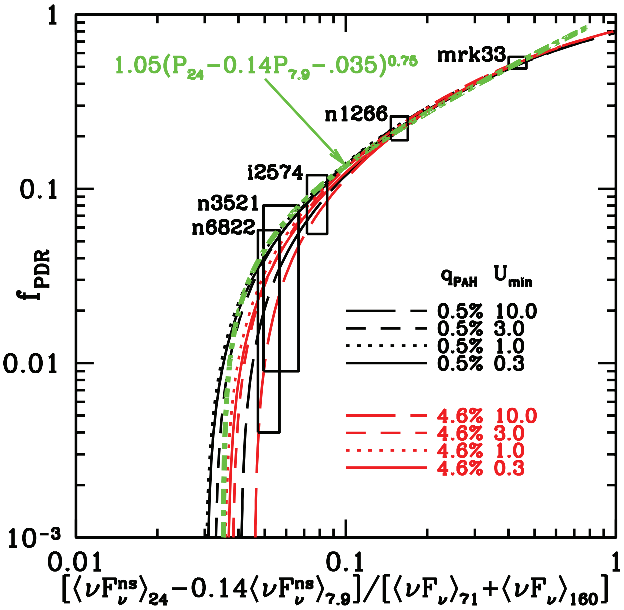

FIG. 22.—Fraction $f_{\rm PDR}$ of the dust IR luminosity radiated by dust grains in regions where $U > 10^2$, plotted as a function of the observable $(P_{24} - 0.14P_{7.9})$. For the five example galaxies, the width of the rectangle corresponds to the $\pm 1\,\sigma$ uncertainty in $P_{24} - 0.14P_{7.9}$. The fitting function $1.05(P_{24} - 0.14P_{7.9} - 0.035)^{0.75}$ approximates the model results.

small PAH ions (see Salama et al. 1996 and references therein). More recent laboratory measurements were carried out by Mattioda et al. (2005b) for 27 PAH cations and anions ranging in size from $C_{14}H_{10}$ to $C_{50}H_{22}$. The newly measured absorption of PAH ions at 0.77–2.5 μm is considerably higher than previously reported. This further supports our earlier conclusion (Li & Draine 2002b) that visible and near-IR photons are able to excite PAHs to temperatures high enough to emit the mid-IR bands, in agreement with the detection of the PAH features in interstellar regions lacking UV photons (Uchida et al. 1998; Pagani et al. 1999),[11] and in agreement with the observation by Sellgren et al. (1990) that the ratio of the *IRAS* 12 μm emission (to which the PAH features are the dominant contributor) to the total FIR surface brightness is independent of the effective temperature $T_{\rm eff}$ of the exciting stars, for 24 reflection nebulae for $5000\ {\rm K} \le T_{\rm eff} \le 33{,}000$ K.

This also relates to our understanding of the origin of interstellar PAHs. At present, the origin and evolution of interstellar PAHs are not very clear. Suggested sources for interstellar PAHs include the injection (into the ISM) of PAHs formed in carbon star outflows (Jura 1987; Latter 1991). However, the PAH emission features are commonly not seen in the mid-IR spectra of C-rich asymptotic giant branch stars. The few C stars that display the PAH features all have a hot companion that emits UV photons (Speck & Barlow 1997; Boersma et al. 2006). It has been suggested that PAHs are present in all C stars but are simply not excited sufficiently to emit at mid-IR due to lack of UV photons. The new visible–IR cross sections for PAH ions (Mattioda et al. 2005b) suggest that PAHs can be excited even by the starlight from a C star, in which case the absence of PAH emission places a limit on the abundance of small PAHs in these outflows.[12]

10.3. *Detectability of* 6.2 μm *Absorption by Interstellar PAHs*

The dust model appropriate to Milky Way dust is thought to have $q_{\rm PAH} \approx 4.6\%$ of the dust mass in PAHs with $N_{\rm C} < 10^3$ C atoms. The carbonaceous grains with $a < 50$ Å contain 52 parts per million (ppm) of C per H nucleon, divided approximately equally between neutral and ionized PAHs. For this model, we predict a 6.22 μm absorption feature with integrated strength

$$\frac{1}{N_{\rm H}} \int \Delta\tau\, d\lambda^{-1} = 6.7 \times 10^{-23} \left(\frac{{\rm C_{PAH}/H}}{52\ {\rm ppm}}\right)\ {\rm cm/H}. \tag{35}$$

Chiar & Tielens (2001) found an upper limit $\int \Delta\tau\, d\lambda^{-1} < 0.8\ {\rm cm}^{-1}$ toward Cyg OB2 No. 12. For the estimated $N_{\rm H} = 1.9 \times 10^{22}\ {\rm cm}^{-2}$, this gives an upper limit

$$\frac{1}{N_{\rm H}} \int \Delta\tau\, d\lambda^{-1} < 4.2 \times 10^{-23}\ {\rm cm/H}, \tag{36}$$

somewhat smaller than our estimate (eq. [35]).

[11] PAH emission features have also been detected in UV-poor dust debris disks around main-sequence stars SAO 206462 (spectral type F8 V, $T_{\rm eff} \approx 6250$ K; Coulson & Walther 1995) and HD 34700 (spectral type G0 V, $T_{\rm eff} \approx 5940$ K; Smith et al. 2004b). However, in an extensive *Spitzer* IRS spectroscopic survey of 111 T Tauri stars in the Taurus star-forming region, Furlan et al. (2006) found that the PAH emission bands are not seen in dust disks around T Tauri stars of spectral type later than G1.

[12] Jura et al. (2006) reported detection of PAH emission features in HD 233517, an evolved oxygen-rich K2 III red giant ($T_{\rm eff} \approx 4390$ K) with circumstellar dust. Jura (2003) argued that the IR excess around HD 233517 is unlikely to be produced by a recent outflow in a stellar wind. Jura et al. (2006) hypothesized that there is a passive, flared disk orbiting HD 233517 and the PAH molecules in the orbiting disk may be synthesized in situ, as well as having been incorporated from the ISM.

TABLE 7
GALAXY EXAMPLES

Parameter	IC 2574	Mrk 33	NGC 1266	NGC 3521	NGC 6822
D (Mpc)	4.02	21.7	31.3	9.0	0.49
$\langle F_\nu \rangle_{3.6}$[a] (Jy)	0.156 ± 0.016	0.027 ± 0.003	0.056 ± 0.006	2.12 ± 0.21	2.20 ± 0.22
$\langle F_\nu \rangle_{7.9}$[a] (Jy)	0.066 ± 0.007	0.125 ± 0.013	0.087 ± 0.009	6.23 ± 0.62	1.41 ± 0.14
$\langle F_\nu \rangle_{24}$[a] (Jy)	0.278 ± 0.013	0.836 ± 0.034	0.861 ± 0.035	5.47 ± 0.22	2.59 ± 0.10
$\langle F_\nu \rangle_{71}$[a] (Jy)	5.10 ± 0.37	3.82 ± 0.28	11.45 ± 0.80	57.2 ± 4.0	59.2 ± 4.2
$\langle F_\nu \rangle_{160}$[a] (Jy)	10.8 ± 1.4	3.63 ± 0.46	9.6 ± 1.2	217. ± 26	143 ± 17
$P_{7.9}$	0.027	0.196	0.0435	0.529	0.065
P_{24}	0.0810	0.460	0.168	0.166	0.061
R_{71}	1.08	2.33	2.55	0.582	0.944
$q_{\rm PAH}$ from Fig. 20 (%)	0.5	3.2	0.5	4.6	1.1
$U_{\rm min}$ from Fig. 21	2.3	7	12.5	1.1	2
γ from Fig. 21	0.012	0.14	0.029	0.007	0.006
$\langle U \rangle$ (from eq. [33])	2.6	18.	16.	1.2	2.1
Ψ [g (ergs s^{-1})$^{-1}$]	0.046	0.061	0.049	0.054	0.0465
$\log(M_{\rm dust}/M_\odot)$	5.79	6.41	7.04	8.10	5.15

[a] Dale et al. (2007).

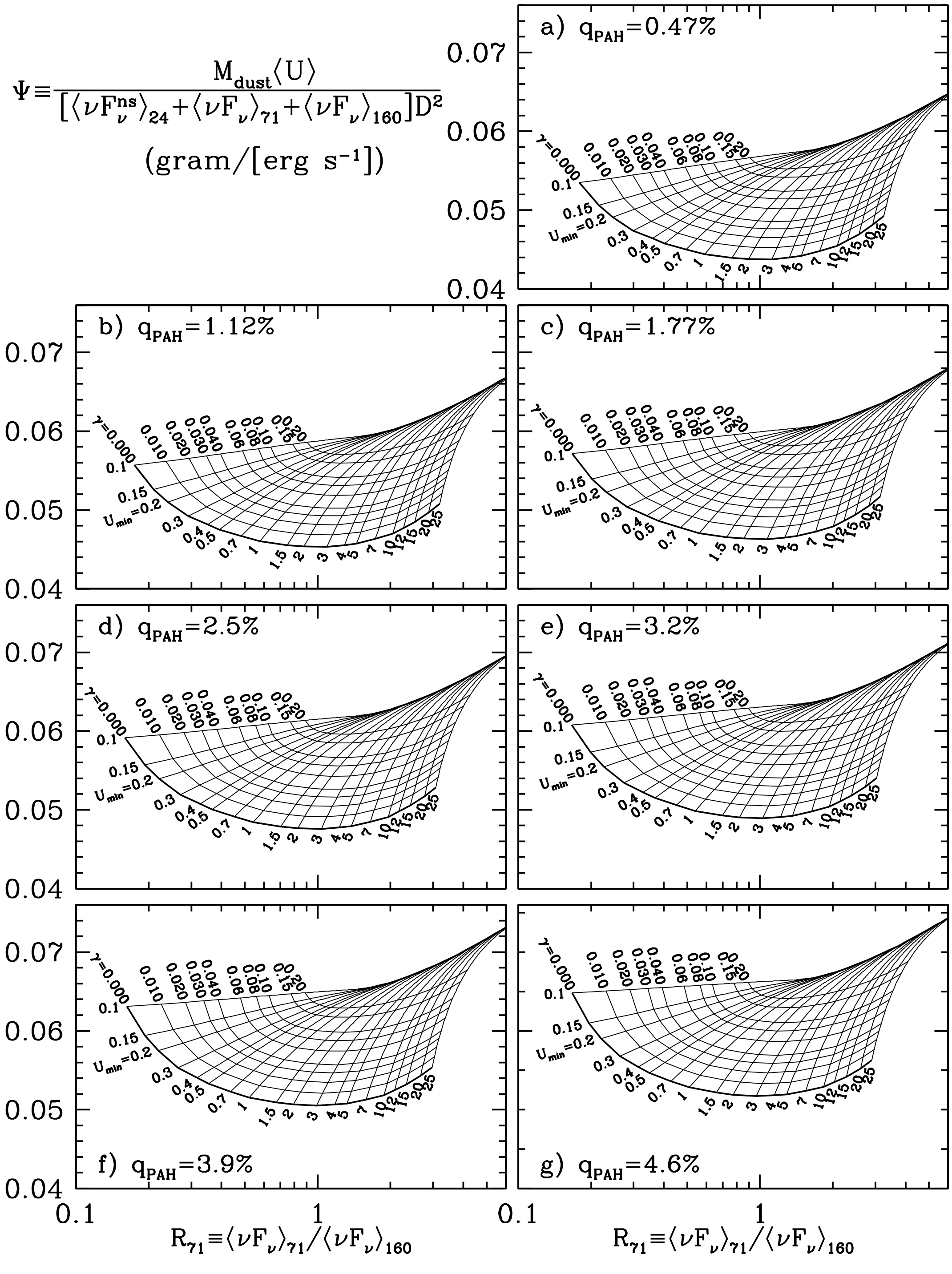

FIG. 23.—Value of Ψ for dust mass estimation (see text).

While the present dust model has 52 ppm C in PAHs with $N_C < 5 \times 10^4$, the 6.22 μm emission is produced mainly by PAHs with $N_C < 500$, which account for only 35 ppm. The 6.2 μm absorption contributed by PAHs with $N_C < 500$ in our model is consistent with the Chiar & Tielens (2001) upper limit.

The absolute PAH band strengths in Table 1 are only estimates. Because the 3–25 μm emission spectrum for $U = 1$ is almost entirely the result of single-photon heating, the emission spectrum would be almost unaffected if all the PAH band strengths were uniformly reduced by a common factor. However, based on the comparison with theoretical calculations shown in Figure 2, the actual band strengths should be similar in magnitude to the values adopted in Table 1. Spectroscopy of heavily extinguished stars using the IRS instrument on *Spitzer* should be carried out to attempt to detect the predicted 6.22 μm absorption from interstellar PAHs.

10.4. *Deuterated PAHs*

Since the aromatic C—D bond zero-point energy is about 30% lower than that of the C—H bond, H loss is favored over D loss. The PAH D/H ratio might therefore be substantially larger than the total D/H $\approx 2 \times 10^{-5}$ (Allamandola et al. 1989b). The observed sight line–to–sight line variations of (D/H) in interstellar gas have been interpreted as requiring depletion of D by interstellar dust (Linsky et al. 2006). Draine (2004, 2006) has suggested that this depletion of D may take place via interactions of PAH ions with the gas and may imply D/H ≈ 0.3 in interstellar PAHs. Peeters et al. (2004) report tentative detection of emission at 4.4 and 4.65 μm from deuterated PAHs from the Orion Bar and M17 PDRs. If the emission is in fact due to C—D stretching modes, Peeters et al. (2004) estimate D/H $\approx 0.17 \pm 0.03$ for the emitting PAHs in the Orion Bar and 0.36 ± 0.08 in M17.

Our model for the PAH absorption cross section is based on observed emission spectra, and some of the modeled absorption may be associated with C—D bending modes if interstellar PAHs are appreciably deuterated. Because the observations of 4.4 and 4.65 μm emission in the Orion Bar and M17 are tentative, we do not attempt here to include any absorption and emission that might result from C—D stretching modes in the 4.5 μm region.

10.5. *Ubiquity and Absence of PAHs in Astrophysical Regions: Rationale for Variable* $q_{\rm PAH}$

The *ISO* and *Spitzer* imaging and spectroscopy have revealed that PAHs are a ubiquitous feature of both the Milky Way and external galaxies. Recent discoveries include the detection of PAH emission in a wide range of systems: distant luminous infrared galaxies (LIRGs) with redshift z ranging from 0.1 to 1.2 (Elbaz et al. 2005); distant ultraluminous infrared galaxies (ULIRGs) with redshift $z \sim 2$ (Yan et al. 2005); distant luminous submillimeter galaxies at redshift $z \sim 2.8$ (Lutz et al. 2005); elliptical galaxies with a hostile environment (containing hot gas of temperature $\sim 10^7$ K), where PAHs can be easily destroyed through sputtering by plasma ions (Kaneda et al. 2005); faint tidal dwarf galaxies with metallicity $\sim Z_\odot/3$ (Higdon et al. 2006); and galaxy halos (Irwin & Madden 2006; Engelbracht et al. 2006).

However, the PAH features are weak or even absent in low-metallicity galaxies and active galactic nuclei (AGNs):

1. Based on an analysis of the mid-IR spectra of 60 galaxies obtained by ground-based observations, Roche et al. (1991) reported the lack of PAH emission features in AGNs.
2. The Small Magellanic Cloud (SMC), an irregular dwarf galaxy with a metallicity just $\sim 1/10$ of solar, exhibits a local minimum at ~ 12 μm in its IR emission spectrum, suggesting the lack of PAHs (Li & Draine 2002c).
3. Thuan et al. (1999), Plante & Sauvage (2002), and Houck et al. (2004) have shown that the PAH features are absent in the *ISO* and *Spitzer* spectra of SBS 0335−052, a metal-poor ($Z \sim Z_\odot/41$) blue compact dwarf galaxy.
4. More recently, Hunt et al. (2005), Madden et al. (2006), and Wu et al. (2006) performed a more systematic investigation of the mid-IR spectra of a large number of low-metallicity galaxies (with $Z/Z_\odot$ ranging from 0.02 to 0.6) obtained with *ISO* and *Spitzer*. They found that the PAH features are substantially suppressed in metal-poor dwarf galaxies.
5. Using *Spitzer* IRAC [3.6] − [7.9] colors and Sloan Digital Sky Survey (SDSS) [$g - r$] colors of 313 visible-selected SDSS main sample galaxies, Hogg et al. (2005) found that low-luminosity galaxies show a deficiency in PAH emission, with weak evidence for a dependence of the PAH-to-stellar radiation ratio on metallicity. Rosenberg et al. (2006) performed a similar study for a statistically complete sample of 19 star-forming dwarf galaxies, but they found a significant number of low-luminosity galaxies with very red [3.6] − [7.9] colors, indicating the presence of PAHs (and/or hot dust). They also found that the 7.9 μm emission is more strongly correlated with the star formation rate than it is with the metallicity.
6. Engelbracht et al. (2005) examined the *Spitzer* mid-IR colors of 34 galaxies ranging over 2 orders of magnitude in metallicity. They found that the 8 μm–to–24 μm color changes abruptly from $F_\nu(8\ \mu{\rm m})/F_\nu(24\ \mu{\rm m}) \sim 0.7$ for galaxies with $Z/Z_\odot > \frac{1}{3}$ to $F_\nu(8\ \mu{\rm m})/F_\nu(24\ \mu{\rm m}) \sim 0.08$ for galaxies with $Z/Z_\odot < \frac{1}{5}$–$\frac{1}{3}$. They attributed this color shift to a decrease in the 7.7 μm PAH feature at low metallicity.
7. The silicate-graphite-PAH model described in this paper has been employed to quantitatively determine the fraction $q_{\rm PAH}$ of the dust mass contributed by PAHs for 61 galaxies in SINGS (Draine et al. 2007). There appears to be a threshold metallicity: galaxies with $[{\rm O/H}] \equiv 12 + \log({\rm O/H}) < 8.1$ (i.e., $Z < Z_\odot/3$) have $q_{\rm PAH} < 1.5\%$.

Knowledge of how $q_{\rm PAH}$ varies as a function of galaxy parameters (such as metallicity, luminosity, and morphological type) will have a broad impact:

1. It will be essential for properly interpreting the IR cosmological surveys that now often assume a *constant* PAH strength for galaxies (see, e.g., Lagache et al. 2004).
2. It may provide physical insight into the validity of using the line-to-continuum ratio of the 7.7 μm PAH feature as a discriminator between starburst and AGN activity in ULIRGs, i.e., whether the dominant luminosity source of ULIRGs is an AGN or a starburst; see Genzel et al. (1998).
3. As local analogs of early galaxies at high redshift that must have formed at very low metallicity, nearby low-metallicity systems can provide insight into the early stages of galaxy evolution. The low PAH abundances observed in these galaxies reflect the balance of PAH formation and destruction and thereby are a valuable probe of the physical conditions following the onset of star formation in primordial gas.
4. By comparing with the star formation rates derived from other tracers, it will allow us to quantitatively evaluate the validity of using the IRAC 8 μm photometry as a reliable tracer for star formation rates. It is generally believed that the IRAC 8 μm flux is stronger in regions with stronger star-forming activities; however, observations suggest that PAHs are destroyed in star-forming regions with very strong and hard radiation fields (Contursi et al. 2000; Förster Schreiber et al. 2004; Beirão et al. 2006).

10.6. *Diversity of PAH Emission Spectra*

The PAH absorption and emission properties presented in this series of papers are for "astronomical" PAHs: we fix the peak wavelength and bandwidth of each PAH band to what is observed in most astronomical regions. The strength of each PAH band (on a per carbon or hydrogen atom basis) is also fixed for a specific charge state to be consistent with what is observed in space, measured in the laboratory, or calculated theoretically.

However, there exist variations in the central wavelength, bandwidth, and strength of PAH emission bands among different astronomical objects or among different locations within one object:

1. Cohen et al. (1989) reported that the central wavelength of the 7.7 μm band varies among different types of objects: it shifts from shorter wavelengths for objects with heavily processed PAHs (e.g., H II regions, reflection nebulae) to longer wavelengths for objects with freshly created PAHs (e.g., planetary nebulae). This wavelength shift has been confirmed by high-resolution spectroscopy obtained with the *ISO* Short Wavelength Spectrometer (SWS; Peeters et al. 2002). Similar shifts have also been seen in other bands (e.g., see van Diedenhoven et al. 2004). More recently, Bregman & Temi (2005) observed a progressive blueshift in the central wavelength of the 7.7 μm band within three reflection nebulae from the edge of the nebulae to places closer to the exciting stars.

2. Uchida et al. (2000) reported a progressive broadening of the FWHM of the 7.7 μm band moving toward the exciting star in the reflection nebula vdB 17. This broadening has also been reported for the reflection nebula Ced 21 (Cesarsky et al. 2000), but such a broadening has not been seen in other PAH bands.

3. Roelfsema et al. (1996) reported that the 8.6 μm band of the compact H II region IRAS 18434−0242 is almost twice as strong as the 7.7 μm band, while for most objects the 7.7 μm band is stronger than the 8.6 μm band by a factor of $\sim$5–10.

4. Reach et al. (2000) reported that the 11.3 μm/7.7 μm band ratio of the PAH emission spectrum of the quiescent molecular cloud SMC B1 No. 1 in the SMC is much higher than that of any other Galactic or extragalactic objects (see Figs. 16 and 17 of Draine & Li 2001).

While the band ratio variations can presumably be accounted for by the combined effects of variations in the radiation exciting the PAHs and variations in PAH sizes and ionization state (small PAHs emit more strongly at the 6.2, 7.7, and 8.6 μm bands, while relatively large PAHs emit more strongly at the 11.3 μm band; neutral PAHs are much stronger 3.3 and 11.3 μm emitters and weaker 6.2, 7.7, and 8.6 μm emitters compared to their charged counterparts), we do not intend to confront our PAH model with extreme spectral variations, such as the observed spectrum of IRAS 18434−024 (with the 8.6 μm band almost twice as strong as the 7.7 μm band), which, according to Roelfsema et al. (1996), is possibly rich in noncompact PAHs. Because of the way we design the astronomical PAH model, the present model is not able to account for the central wavelength shifts and the 7.7 μm band broadening, although experimental investigations have been carried out (e.g., see Hudgins & Allamandola 1999).

Hudgins & Allamandola (2005) discuss recent work toward PAH identification, with attention to the effects of N substitution. Future, more realistic modeling will require more extensive knowledge of PAH properties than is now available from laboratory studies (e.g., Hudgins & Allamandola 1999; Mattioda et al. 2005a, 2005b) and theoretical calculations (e.g., Bakes et al. 2001a, 2001b; Malloci et al. 2004, 2007; Mulas et al. 2006).

10.7. *Other Grain Models*

The dust model used in this study is, of course, provisional. The model assumes the amorphous silicate and carbonaceous material to be in physically separate grains. While this appears to be consistent with observations, including the observed absence of polarization in the 3.4 μm absorption feature (Chiar et al. 2006), it is by no means observationally established.

Our models have also used the dielectric tensor of crystalline graphite to estimate the infrared absorption by carbonaceous grains with $a \gtrsim 0.01$ μm. Some form of amorphous carbon may provide a better approximation for interstellar carbonaceous material that may be formed from agglomeration of PAHs followed by cross linking due to ultraviolet photolysis and cosmic-ray exposure. The main effect on the present models would be to do away with the broad absorption feature near 30 μm that appears in the calculated $C_{\rm abs}(\lambda)$ for graphitic material, as seen in Figure 3, and the corresponding broad emission feature near 30 μm when the starlight intensity is high enough to heat $a \gtrsim 0.01$ μm carbonaceous grains to $T \gtrsim 10^2$ K.

In this work we focus on the silicate-graphite-PAH model. For other dust models, if they are tailored to reproduce the Milky Way interstellar extinction *and* albedo in the optical/UV *and* meanwhile satisfy plausible interstellar abundance constraints, the derived parameters $M_{\rm dust}\langle U \rangle$ will be nearly the same as derived from the silicate-graphite-PAH model, simply from energy balance considerations: the energy emitted in the IR must be absorbed by the same dust in the optical/UV. If the dust model reproduces the observed FIR emission spectrum of Milky Way dust for $U \approx 1$, then the temperatures of the larger dust grains will scale with changes in U in a manner similar to the present model, and therefore the inferred properties of the radiation field ($U_{\rm min}$, γ) will presumably be similar.

However, the composite model will probably have a lower optical/UV albedo than observed (Dwek 1997). Because the extinction per H atom is fixed by observations, the lower albedo will result in more total FIR emission per H nucleon. Given the uncertainties regarding both the intensity of interstellar starlight and the FIR emission from dust, composite grain models must be considered to be viable. Additional observational tests to distinguish between dust models are needed.

11. SUMMARY

The principal results of this study are as follows:

1. The wavelength dependence of absorption by interstellar PAHs has been revised to better reproduce observed emission spectra. The adopted $C_{\rm abs}(\lambda)$ are generally consistent with measured or calculated absorption cross sections for PAHs (Fig. 2).

2. Temperature distribution functions have been calculated for PAHs of different sizes, heated by starlight with the spectrum estimated for the local interstellar radiation field. These temperature distribution functions have been used to compute the time-averaged emission spectra for PAHs of different sizes (Fig. 5).

3. Figures 6 and 7 show the efficiency with which PAHs radiate absorbed energy into different emission features. The strong 7.7 μm feature is radiated efficiently only by PAHs with $N_{\rm C} \lesssim 10^3$ carbon atoms: larger PAHs radiate primarily at longer wavelengths.

4. Emission spectra have been calculated for dust models that reproduce the average Milky Way extinction, using size distributions with different abundances of small PAHs (see Fig. 12).

5. Emission spectra have been calculated for dust mixtures heated by different starlight intensities (see Fig. 13).

6. The dust model used in this paper is found to be in good agreement with observed IRAC 3.6 μm/IRAC 7.9 μm and IRAC 5.7 μm/IRAC 7.9 μm band ratios (see Fig. 16) but underpredicts the observed IRAC 4.5 μm/IRAC 7.9 μm ratio by about a factor of 1.5.

7. The FIR and submillimeter emission spectrum calculated for the present model appears to be in good agreement with the observed emission from dust in the local Milky Way (see Fig. 14).

8. A prescription (eq. [17]) is found that allows the total IR emission to be estimated from observed fluxes in the IRAC 7.9 μm band and the three MIPS bands. For dust heated by starlight intensities $0.1 < U \lesssim 10^2$, equation (17) is accurate to within $\sim$10%.

9. Emission spectra have been calculated for dust mixtures heated by power-law distributions of starlight intensities (see Fig. 18).

10. A distribution function (eq. [23]) is proposed for representing the distribution of starlight intensities heating dust in a galaxy or region within a galaxy.

11. Graphical procedures are presented that allow dust model parameters to be found using three ratios ($P_{7.9}$, P_{24}, and R_{71}) constructed from fluxes measured in IRAC band 4 and MIPS bands 1–3. The graphs provided here (Figs. 20 and 21) allow model parameters $q_{\rm PAH}$, $U_{\rm min}$, and γ to be estimated.

12. The fraction f_{PDR} of the dust infrared emission that is contributed by dust in PDRs with $U > 10^2$ can be estimated from IRAC and MIPS photometry using Figure 22.

13. Using a coefficient Ψ obtained from Figure 23, the total dust mass M_{dust} can be estimated from fluxes in the three MIPS bands using equation (34).

We are grateful to G. Malloci for making available to us theoretical absorption cross sections for a number of PAHs in advance of publication; to E. Peeters for providing SWS spectra of the Orion Bar, M17, and NGC 7027; to K. Sellgren for providing IRS spectra of NGC 7023; to T. Onaka for providing response functions for Akari; and to A. Poglitsch and M. Griffin for providing response functions for PACS and SPIRE. We thank the referee, G. Clayton, for helpful comments. B. T. D. was supported in part by NSF grant AST 04-06883. A. L. is supported in part by the University of Missouri Summer Research Fellowship, the University of Missouri Research Board, and NASA/*Spitzer* Theory Programs. We are grateful to R. H. Lupton for availability of the SM graphics program, used extensively in preparation of this paper.

REFERENCES

Adamson, A. J., Whittet, D. C. B., Chrysostomou, A., Hough, J. H., Aitken, D. K., Wright, G. S., & Roche, P. F. 1999, ApJ, 512, 224
Allamandola, L. J., Bregman, J. D., Sandford, S. A., Tielens, A. G. G. M., Witteborn, F. C., Wooden, D. H., & Rank, D. 1989a, ApJ, 345, L59
Allamandola, L. J., Tielens, A. G. G. M., & Barker, J. R. 1985, ApJ, 290, L25
———. 1989b, ApJS, 71, 733
An, J. H., & Sellgren, K. 2003, ApJ, 599, 312
Asplund, M., Grevesse, N., Sauval, A. J., Allende Prieto, C., & Kiselman, D. 2004, A&A, 417, 751
Bakes, E. L. O., Tielens, A. G. G. M., & Bauschlicher, Jr., C. W. 2001a, ApJ, 556, 501
Bakes, E. L. O., Tielens, A. G. G. M., Bauschlicher, Jr., C. W., Hudgins, D. M., & Allamandola, L. J. 2001b, ApJ, 560, 261
Beintema, D. A., et al. 1996, A&A, 315, L369
Beirão, P., Brandl, B. R., Devost, D., Smith, J. D., Hao, L., & Houck, J. R. 2006, ApJ, 643, L1
Boersma, C., Hony, S., & Tielens, A. G. G. M. 2006, A&A, 447, 213
Boulanger, F., Abergel, A., Cesarsky, D., Bernard, J. P., Miville Deschênes, M. A., Verstraete, L., & Reach, W. T. 2000, in *ISO* beyond Point Sources, ed. R. J. Laureijs, K. Leech, & M. F. Kessler (ESA-SP 455; Madrid: ESA), 91
Boulanger, F., Boissel, P., Cesarsky, D., & Ryter, C. 1998, A&A, 339, 194
Bregman, J., & Temi, P. 2005, ApJ, 621, 831
Cartledge, S. I. B., Lauroesch, J. T., Meyer, D. M., & Sofia, U. J. 2006, ApJ, 641, 327
Cesarsky, D., Lequeux, J., Ryter, C., & Gérin, M. 2000, A&A, 354, L87
Chiar, J. E., & Tielens, A. G. G. M. 2001, ApJ, 550, L207
Chiar, J. E., et al. 2006, ApJ, 651, 268
Cohen, M., Tielens, A. G. G. M., Bregman, J., Witteborn, F. C., Rank, D. M., Allamandola, L. J., Wooden, D., & Jourdain de Muizon, M. 1989, ApJ, 341, 246
Contursi, A., et al. 2000, A&A, 362, 310
Coulson, I. M., & Walther, D. M. 1995, MNRAS, 274, 977
Cunha, K., Hubeny, I., & Lanz, T. 2006, ApJ, 647, L143
Dale, D. A., & Helou, G. 2002, ApJ, 576, 159
Dale, D. A., Helou, G., Contursi, A., Silbermann, N. A., & Kolhatkar, S. 2001, ApJ, 549, 215
Dale, D. A., et al. 2005, ApJ, 633, 857
———. 2007, ApJ, 655, 863
Désert, F.-X., Boulanger, F., & Puget, J. L. 1990, A&A, 237, 215
Draine, B. T. 1994, in ASP Conf. Ser. 58, The First Symposium on the Infrared Cirrus and Diffuse Interstellar Clouds, ed. R. M. Cutri & W. B. Latter (San Francisco: ASP), 227
———. 2003, ARA&A, 41, 241
———. 2004, in Origin and Evolution of the Elements, ed. A. McWilliam & M. Rauch (Cambridge: Cambridge Univ. Press), 317
———. 2006, in ASP Conf. Ser. 348, Astrophysics in the Far Ultraviolet, ed. G. Sonneborn, H. Moos, & B.-G. Andersson (San Francisco: ASP), 58
Draine, B. T., & Lee, H. M. 1984, ApJ, 285, 89
Draine, B. T., & Li, A. 2001, ApJ, 551, 807
Draine, B. T., et al. 2007, ApJ, submitted
Duley, W. W., & Williams, D. A. 1981, MNRAS, 196, 269
Dwek, E. 1997, ApJ, 484, 779
Elbaz, D., Le Floc'h, E., Dole, H., & Marcillac, D. 2005, A&A, 434, L1
Engelbracht, C. W., Gordon, K. D., Rieke, G. H., Werner, M. W., Dale, D. A., & Latter, W. B. 2005, ApJ, 628, L29
Engelbracht, C. W., et al. 2006, ApJ, 642, L127
Finkbeiner, D. P., Davis, M., & Schlegel, D. J. 1999, ApJ, 524, 867 (FDS99)
Flagey, N., Boulanger, F., Verstraete, L., Miville Deschenes, M. A., Noriega Crespo, A., & Reach, W. T. 2006, A&A, 453, 969
Förster Schreiber, N. M., Roussel, H., Sauvage, M., & Charmandaris, V. 2004, A&A, 419, 501
Furlan, E., et al. 2006, ApJS, 165, 568
Genzel, R., et al. 1998, ApJ, 498, 579
Helou, G., et al. 2004, ApJS, 154, 253
Higdon, S. J., Higdon, J. L., & Marshall, J. 2006, ApJ, 640, 768
Hogg, D. W., Tremonti, C. A., Blanton, M. R., Finkbeiner, D. P., Padmanabhan, N., Quintero, A. D., Schlegel, D. J., & Wherry, N. 2005, ApJ, 624, 162
Houck, J. R., et al. 2004, ApJS, 154, 211
Hudgins, D. M., & Allamandola, L. J. 1999, ApJ, 513, L69
———. 2005, in IAU Symp. 231, Astrochemistry, ed. D. C. Lis, G. A. Blake, & E. Herbst (Cambridge: Cambridge Univ. Press), 443
Hunt, L., Bianchi, S., & Maiolino, R. 2005, A&A, 434, 849
Irwin, J. A., & Madden, S. C. 2006, A&A, 445, 123
Joblin, C., Abergel, A., Bregman, J., D'Hendecourt, L., Heras, A. M., Jourdain de Muizon, M., Pech, C., & Tielens, A. G. G. M. 2000, in *ISO* beyond the Peaks, ed. A. Salama et al. (ESA-SP 456; Madrid: ESA), 49
Jones, A. P., & d'Hendecourt, L. 2000, A&A, 355, 1191
Jones, A. P., Duley, W. W., & Williams, D. A. 1990, QJRAS, 31, 567
Jura, M. 1987, in Polycyclic Aromatic Hydrocarbons and Astrophysics, ed. A. Leger, L. D'Hendecourt, & N. Boccara (NATO ASI Ser. C, 191; Dordrecht: Reidel), 3
———. 2003, ApJ, 582, 1032
Jura, M., et al. 2006, ApJ, 637, L45
Kahanpää, J., Mattila, K., Lehtinen, K., Leinert, C., & Lemke, D. 2003, A&A, 405, 999
Kaneda, H., Onaka, T., & Sakon, I. 2005, ApJ, 632, L83
Kawada, M., Shibai, H., Kaneda, H., & Nakagawa, T. 2004, Proc. SPIE, 5487, 359
Kim, S.-H., Martin, P. G., & Hendry, P. D. 1994, ApJ, 422, 164
Lagache, G., et al. 2004, ApJS, 154, 112
Latter, W. B. 1991, ApJ, 377, 187
Leger, A., & Puget, J. L. 1984, A&A, 137, L5
Li, A. 2005, ApJ, 622, 965
Li, A., & Draine, B. T. 2001a, ApJ, 550, L213
———. 2001b, ApJ, 554, 778 (LD01)
———. 2002a, ApJ, 564, 803
———. 2002b, ApJ, 572, 232
———. 2002c, ApJ, 576, 762
Li, A., & Greenberg, J. M. 1997, A&A, 323, 566
Li, A., & Greenberg, J. M. 2002, ApJ, 577, 789
Linsky, J. L., et al. 2006, ApJ, 647, 1106
Lu, N., et al. 2003, ApJ, 588, 199
Lutz, D., Valiante, E., Sturm, E., Genzel, R., Tacconi, L. J., Lehnert, M. D., Sternberg, A., & Baker, A. J. 2005, ApJ, 625, L83
Madden, S. C., Galliano, F., Jones, A. P., & Sauvage, M. 2006, A&A, 446, 877
Malloci, G., Joblin, C., & Mulas, G. 2007, Chem. Phys., 332, 353
Malloci, G., Mulas, G., & Joblin, C. 2004, A&A, 426, 105
Mason, R. E., Wright, G. S., Adamson, A., & Pendleton, Y. 2007, ApJ, in press
Mathis, J. S. 1996, ApJ, 472, 643
Mathis, J. S., Mezger, P. G., & Panagia, N. 1983, A&A, 128, 212
Mathis, J. S., Rumpl, W., & Nordsieck, K. H. 1977, ApJ, 217, 425
Mathis, J. S., & Whiffen, G. 1989, ApJ, 341, 808
Mattioda, A. L., Allamandola, L. J., & Hudgins, D. M. 2005a, ApJ, 629, 1183
Mattioda, A. L., Hudgins, D. M., & Allamandola, L. J. 2005b, ApJ, 629, 1188
Mennella, V., Brucato, J. R., Colangeli, L., & Palumbo, P. 1999, ApJ, 524, L71
Moutou, C., Leger, A., & D'Hendecourt, L. 1996, A&A, 310, 297
Moutou, C., Sellgren, K., Verstraete, L., & Léger, A. 1999, A&A, 347, 949
Mulas, G., Malloci, G., Joblin, C., & Toublanc, D. 2006, A&A, 460, 93
Onaka, T., Yamamura, I., Tanabe, T., Roellig, T. L., & Yuen, L. 1996, PASJ, 48, L59
Onaka, T., et al. 2004, Proc. SPIE, 5487, 338

Pagani, L., Lequeux, J., Cesarsky, D., Donas, J., Milliard, B., Loinard, L., & Sauvage, M. 1999, A&A, 351, 447
Papoular, R., Ellis, K., Guillois, O., Reynaud, C., & Nenner, I. 1993, J. Chem. Soc. Faraday Trans., 89, 2289
Peeters, E., Allamandola, L. J., Bauschlicher, Jr., C. W., Hudgins, D. M., Sandford, S. A., & Tielens, A. G. G. M. 2004, ApJ, 604, 252
Peeters, E., Hony, S., Van Kerckhoven, C., Tielens, A. G. G. M., Allamandola, L. J., Hudgins, D. M., & Bauschlicher, C. W. 2002, A&A, 390, 1089
Peeters, E., Tielens, A. G. G. M., Boogert, A. C. A., Hayward, T. L., & Allamandola, L. J. 2005, ApJ, 620, 774
Piovan, L., Tantalo, R., & Chiosi, C. 2006, MNRAS, 366, 923
Plante, S., & Sauvage, M. 2002, AJ, 124, 1995
Popescu, C. C., Misiriotis, A., Kylafis, N. D., Tuffs, R. J., & Fischera, J. 2000, A&A, 362, 138
Reach, W. T., Boulanger, F., Contursi, A., & Lequeux, J. 2000, A&A, 361, 895
Roche, P. F., Aitken, D. K., Smith, C. H., & Ward, M. J. 1991, MNRAS, 248, 606
Roelfsema, P. R., et al. 1996, A&A, 315, L289
Rosenberg, J. L., Ashby, M. L. N., Salzer, J. J., & Huang, J.-S. 2006, ApJ, 636, 742
Sakata, A., Wada, S., Onaka, T., & Tokunaga, A. T. 1987, ApJ, 320, L63
Sakon, I., Onaka, T., Ishihara, D., Ootsubo, T., Yamamura, I., Tanabé, T., & Roellig, T. L. 2004, ApJ, 609, 203
Salama, F., Bakes, E. L. O., Allamandola, L. J., & Tielens, A. G. G. M. 1996, ApJ, 458, 621
Sellgren, K., Luan, L., & Werner, M. W. 1990, ApJ, 359, 384
Siebenmorgen, R., & Krügel, E. 1992, A&A, 259, 614
Silva, L., Granato, G. L., Bressan, A., & Danese, L. 1998, ApJ, 509, 103
Smith, J. D. T., et al. 2004a, ApJS, 154, 199
———. 2007, ApJ, 656, 770
Smith, T. L., Clayton, G. C., & Valencic, L. 2004b, AJ, 128, 357
Snow, T. P. 2000, J. Geophys. Res., 105, 10239
Snow, T. P., & Witt, A. N. 1996, ApJ, 468, L65
Speck, A. K., & Barlow, M. J. 1997, Ap&SS, 251, 115
Tanabe, T., Nakada, Y., Kamijo, F., & Sakata, A. 1983, PASJ, 35, 397
Tanaka, M., Matsumoto, T., Murakami, H., Kawada, M., Noda, M., & Matsuura, S. 1996, PASJ, 48, L53
Thuan, T. X., Sauvage, M., & Madden, S. 1999, ApJ, 516, 783
Tielens, A. G. G. M. 2005, The Physics and Chemistry of the Interstellar Medium (Cambridge: Cambridge Univ. Press)
Tielens, A. G. G. M., Hony, S., van Kerckhoven, C., & Peeters, E. 1999, in The Universe as Seen by *ISO*, ed. P. Cox & M. F. Kessler (ESA-SP 427; Noordwijk: ESA), 579
Tuffs, R. J., Popescu, C. C., Völk, H. J., Kylafis, N. D., & Dopita, M. A. 2004, A&A, 419, 821
Uchida, K. I., Sellgren, K., & Werner, M. 1998, ApJ, 493, L109
Uchida, K. I., Sellgren, K., Werner, M. W., & Houdashelt, M. L. 2000, ApJ, 530, 817
van Diedenhoven, B., Peeters, E., Van Kerckhoven, C., Hony, S., Hudgins, D. M., Allamandola, L. J., & Tielens, A. G. G. M. 2004, ApJ, 611, 928
Verstraete, L., Puget, J. L., Falgarone, E., Drapatz, S., Wright, C. M., & Timmermann, R. 1996, A&A, 315, L337
Verstraete, L., et al. 2001, A&A, 372, 981
Webster, A. 1993, MNRAS, 264, 121
Weingartner, J. C., & Draine, B. T. 2001a, ApJ, 548, 296 (WD01)
———. 2001b, ApJS, 134, 263
Werner, M. W., Uchida, K. I., Sellgren, K., Marengo, M., Gordon, K. D., Morris, P. W., Houck, J. R., & Stansberry, J. A. 2004a, ApJS, 154, 309
Werner, M. W., et al. 2004b, ApJS, 154, 1
Witt, A. N., & Gordon, K. D. 1996, ApJ, 463, 681
Wu, Y., Charmandaris, V., Hao, L., Brandl, B. R., Bernard-Salas, J., Spoon, H. W. W., & Houck, J. R. 2006, ApJ, 639, 157
Yan, L., et al. 2005, ApJ, 628, 604
Zhou, Z., Sfeir, M. Y., Zhang, L., Hybertsen, M. S., Steigerwald, M., & Brus, L. 2006, ApJ, 638, L105
Zubko, V., Dwek, E., & Arendt, R. G. 2004, ApJS, 152, 211